HHS Public Access

Author manuscript

Cell. Author manuscript; available in PMC 2019 October 04.

Published in final edited form as:

Cell. 2018 October 04; 175(2): 472–487.e20. doi:10.1016/j.cell.2018.07.043.

Anatomically Defined and Functionally Distinct Dorsal Raphe Serotonin Sub-systems

Jing Ren[1], **Drew Friedmann**[1], **Jing Xiong**[2], **Cindy D. Liu**[1], **Brielle R. Ferguson**[3], **Tanya Weerakkody**[3], **Katherine E. DeLoach**[1], **Chen Ran**[1], **Albert Pun**[1], **Yanwen Sun**[4], **Brandon Weissbourd**[1], **Rachael L. Neve**[5], **John Huguenard**[3], **Mark A. Horowitz**[2], and **Liqun Luo**[1,*]

[1]Department of Biology and Howard Hughes Medical Institute, Stanford University, Stanford, CA 94305, USA

[2]Department of Electrical Engineering, Stanford University, Stanford, CA 94305, USA

[3]Department of Neurology and Neurological Sciences, Stanford University, Stanford, CA 94305, USA

[4]Department of Physics, Stanford University, Stanford, CA 94305, USA

[5]Delivery Technology Core, Massachusetts General Hospital, Cambridge, MA 02139, USA.

Summary

The dorsal raphe (DR) constitutes a major serotonergic input to the forebrain and modulates diverse functions and brain states including mood, anxiety, and sensory and motor functions. Most functional studies to date have treated DR serotonin neurons as a single population. Using viral-genetic methods, we found that subcortical- and cortical-projecting serotonin neurons have distinct cell body distributions within the DR and differentially co-express a vesicular glutamate transporter. Further, amygdala- and frontal cortex-projecting DR serotonin neurons have largely complementary whole-brain collateralization patterns, receive biased inputs from presynaptic partners, and exhibit opposite responses to aversive stimuli. Gain- and loss-of-function experiments suggest that amygdala-projecting DR serotonin neurons promote anxiety-like behavior, whereas frontal cortex-projecting neurons promote active coping in the face of challenge. These results provide compelling evidence that the DR serotonin system contains parallel sub-systems that differ in input and output connectivity, physiological response properties, and behavioral functions.

In brief:

*Correspondence and lead contact: lluo@stanford.edu.

Author Contributions: J.R. designed and performed most of the experiments. D.F. performed iDISCO+ imaging and analysis. J.X. and M.A.H. developed image registration algorithm. B.R.F., T.W., and J.H. performed local field potential recordings and data analyses. C.D.L., K.E.D., C.R., A.P., Y.S. and B.W. assisted in experiments or data analyses. R.L.N. produced HSV reagents. L.L. supervised the project. J.R. and L.L. wrote the manuscript with contributions from all coauthors.

Declaration of Interests

The authors declare no competing interests.

Two highly complementary parallel serotonergic neuronal pathways in the brain projecting from the dorsal raphe to cortical and subcortical regions of the brain are each activated by reward but show opposite responses to aversive stimuli.

Abstract

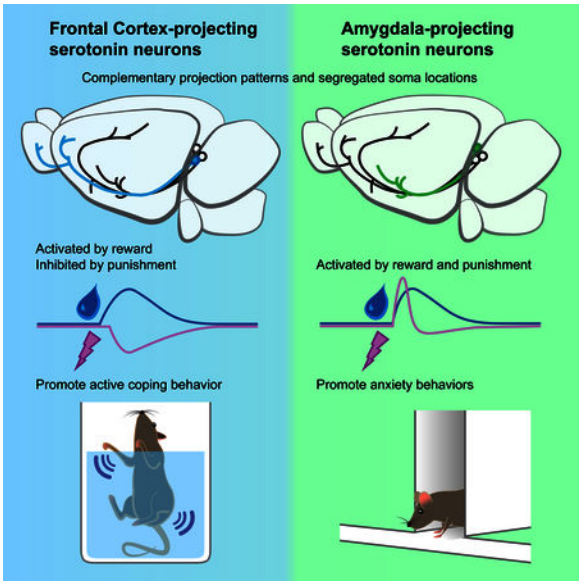

Introduction

The serotonin system powerfully modulates physiology and behavior in health and disease. It is the most widely used pharmacological target for treating depression and anxiety (Belmaker and Agam, 2008; Ravindran and Stein, 2010), and depression has become the leading cause of disability worldwide (World Health Organization, 2017). However, a physiological and circuitry-based theory of how the serotonin system is organized to carry out its diverse functions remains elusive (Dayan and Huys, 2015; Muller and Jacobs, 2010).

Serotonergic fibers originate from a few discrete nuclei in the brainstem but innervate the entire mammalian brain (Steinbusch, 1981). The dorsal raphe nucleus (DR) contains ~35% of ~26,000 serotonin-producing neurons in the mouse brain and is the predominant source of serotonergic innervation of the forebrain (Ishimura et al., 1988). Despite a large body of literature (Muller and Jacobs, 2010), a consensus on the primary functions of the DR serotonin system is lacking. For example, recent studies on the effects of acute activation of DR serotonin neurons have reported divergent findings, including reinforcement (Liu et al., 2014), promotion of waiting for delayed reward rather than reinforcement (Fonseca et al., 2015; Miyazaki et al., 2012), promotion of anxiety-like behaviors and suppression of locomotion (Teissier et al., 2015; Urban et al., 2016), and suppression of locomotion without effects on reinforcement or anxiety-like behaviors (Correia et al., 2017). While different behavioral assays and activation methods may contribute to these conflicting results, they may also stem from treating the DR serotonin system as a monolithic whole.

Accumulating evidence points to physiological and molecular heterogeneity within the DR serotonin system (Calizo et al., 2011; Cohen et al., 2015; Fernandez et al., 2016; Okaty et al., 2015). Based on retrograde tracing DR subregions may preferentially project to different targets (reviewed in Waselus et al., 2011). Whole-brain input mapping suggested heterogeneity of DR serotonin neurons has also been implicated with respect to presynaptic inputs (Weissbourd et al., 2014). Recent studies have begun to target DR subpopulations by utilizing optogenetic activation of serotoninergic terminals at specific targets (Marcinkiewcz et al., 2016) or genetic intersection combined with chemogenetic perturbations (Niederkofler et al., 2016). However, given the scale and complexity, comprehensive characterizations that integrate anatomy, physiology, and function are essential for understanding how DR serotonin system is organized to modulate diverse physiological and behavioral functions. Here, we used a combination of viral-genetic approaches to dissect the DR serotonin system with respect to projection targets, synaptic input, physiological responses, and behavioral functions.

Results

DR Serotonin Neurons that Project to Specific Targets Have Stereotyped Locations

To determine if the spatial distribution of DR serotonin neurons correlates with their projection targets, we performed retrograde tracing combined with serotonin marker staining at the DR. We sampled eight brain regions previously reported to be heavily innervated by DR projections (Allen Brain Atlas, 2017; Oh et al., 2014; Vertes, 1991): the paraventricular hypothalamic nucleus (PVH), central amygdala (CeA), lateral habenula (LHb), dorsal lateral geniculate nucleus (dLGN), olfactory bulb (OB), orbitofrontal cortex (OFC), piriform cortex (PIR), and entorhinal cortex (ENT) (n=4 per region). We injected *HSV-Cre* (Neve et al., 2005), which transduces neurons via their axon terminals, unilaterally into these regions in *Ai14* tdTomato Cre reporter mice (Madisen et al., 2010) (Figure 1A; Figure S1A). Co-staining of DR sections with tryptophan hydroxylase 2 (Tph2) revealed that serotonin neurons projecting to specific output sites have stereotyped cell body locations in the DR. Specifically, serotonin neurons projecting to subcortical regions localized more in the dorsal DR, whereas those that project to the OB and three cortical areas preferentially localized in the ventral DR (Figure 1B).

For quantitative analysis, we developed an algorithm to register all DR-containing histological sections to the Allen Institute reference brain (Figure 1A, right panels; Figure S1B–E; STAR Methods; Xiong et al., 2018). We then created clusters using the combined data from four brains with the same injection sites (Figure 1B, right insets). We found that serotonin neurons projecting to the four subcortical sites appeared largely overlapping, which we combined to produce a subcortical cluster ($DR^{Tph2}\rightarrow SC$) (Figure 1C). Likewise, serotonin neurons projecting to the OB, PIR, and OFC also exhibited considerable overlap, which we combined to produce an anterior cortical cluster ($DR^{Tph2}\rightarrow AC$). ENT-projecting serotonin neurons tended to distribute more caudally than other populations. $DR^{Tph2}\rightarrow SC$ and $DR^{Tph2}\rightarrow AC$ clusters preferentially occupied dorsal and ventral DR, respectively, albeit with partial overlaps that accounted for 17.4% of the $DR^{Tph2}\rightarrow SC$ volume and 39.6% of the $DR^{Tph2}\rightarrow AC$ volume (Figure $1C_3$–C_4, Figure S1E–H). We also performed dual-color

retrograde tracing to determine if individual DR serotonin neurons target to multiple areas. While the low efficiency of co-labeling even for two tracers sequentially injected at the same site prevented us from making strong conclusions, our data was nevertheless consistent with OFC-projecting DR serotonin neurons had more overlap with OB-projecting ones than with CeA-projecting ones (Figure S1I). These data demonstrate that the cell bodies of DR serotonin neurons are organized according to their projection patterns (see Movie S1 for a summary).

DR Serotonin Neurons that Co-express Vglut3 Preferentially Project to Cortical Regions

~60% of DR serotonin neurons co-express the vesicular glutamate transporter Vglut3 in the rat (Gras et al., 2002) and co-release glutamate in the mouse (Liu et al., 2014; Sengupta et al., 2017). To investigate the distribution of dual-transmitter-containing ($DR^{Vglut3\&Tph2}$) neurons, we crossed *Vglut3-Cre* mice (Grimes et al., 2011) with the *Ai14* reporter and stained DR sections with Tph2. We found that Vglut3 also subdivided the DR serotonin neurons roughly into dorsal and ventral compartments (Figure 1D). After registering three double-labeled brains to produce the $DR^{Vglut3\&Tph2}$ cluster, we found that it had 66%±0.6% (mean±SEM) overlap with the $DR^{Tph2}\rightarrow$AC but only 19%±1.1% overlap with the $DR^{Tph2}\rightarrow$SC cluster (Figure 1E; Movie S1).

These data suggest that serotonin neurons that project to the OB and cortical regions more likely co-express Vglut3. To verify this, we injected GFP-expressing rabies virus as a retrograde tracer (Wickersham et al., 2007) into the above eight brain regions of *Vglut3-Cre;Ai14* mice, and determined the percentage of $GFP^+/tdTomato^+/Tph2^+$ triple-labeled cells within the $GFP^+/Tph2^+$ double-labeled population (Figure 1F). Indeed, many OB- and cortical-projecting serotonin neurons were $Vglut3^+$, whereas subcortical-projecting serotonin neurons were mostly $Vglut3^-$ (Figure 1G). Thus, the DR serotonin system has a coordinated spatial and neurochemical organization with respect to its projection targets, although these subdivisions are not absolute.

OFC- and CeA-projecting DR Serotonin Neurons Have Largely Complementary Collateralization Patterns

A key question is to what extent serotonin neurons that project to one target region collateralize to other brain regions. Given the apparent distinction of cortical- and subcortical-projecting DR serotonin neurons (Figure 1), we used an intersectional strategy (Beier et al., 2015; Schwarz et al., 2015) to examine the collateralization patterns of OFC- and CeA- projecting ones as examples. Into *Sert-Cre* mice (Gong et al., 2007) that express Cre recombinase in cells expressing the serotonin transporter (Sert), we injected an axon-terminal-transducing AAV (Tervo et al., 2016) expressing Cre-dependent Flp recombinase (AAV_{retro}-$FLEx^{loxP}$-*Flp)* at the OFC or CeA, and AAVs expressing Flp-dependent membrane tethered GFP (*AAV-*$FLEx^{FLP}$*-mGFP*) at the DR (Figure 2A). We then employed iDISCO+ (Renier et al., 2016) to clear the brain in a whole-mount preparation, registered the imaged volume from light-sheet imaging to the Allen reference brain, and examined resultant axonal arborization patterns (STAR Methods).

We analyzed the projection patterns of DR serotonin neurons labeled retrogradely from either the OFC or CeA (abbreviated as $DR^{Sert}\rightarrow$OFC and $DR^{Sert}\rightarrow$CeA neurons hereafter) in four brains each (Figure 2; Figure S2; Table S1). 3D rendering suggested that $DR^{Sert}\rightarrow$OFC and $DR^{Sert}\rightarrow$CeA axons exhibited complementary whole-brain projection patterns, preferentially innervating superficial (cortical) and deep (subcortical) regions (Figure 2B; Movie S2; Table S1). Examination in thin optical sections revealed the stereotypy of individual brains from the same group despite notable differences in labeling intensity (Figure 2C–E). For example, the OFC and OB were intensively innervated by $DR^{Sert}\rightarrow$OFC axons but lacked $DR^{Sert}\rightarrow$CeA axons (Figure S2A). By contrast, the CeA, PVH, ventral bed nucleus of stria terminalis (BNST), and substantia nigra were innervated by $DR^{Sert}\rightarrow$CeA axons but lacked $DR^{Sert}\rightarrow$OFC axons (Figure 2G; Figure S2B). $DR^{Sert}\rightarrow$CeA axons also innervated the lateral amygdala, basolateral amygdala, and intercalated nucleus of the amygdala (Table S1). However, the nearby cortical amygdala was innervated mostly by $DR^{Sert}\rightarrow$OFC axons (Figure S2A).

Whole-brain quantitative and statistical analyses of $DR^{Sert}\rightarrow$OFC and $DR^{Sert}\rightarrow$CeA axonal projections confirmed that the innervation patterns were largely complementary throughout the brain (Figure 2F–G; Movie S3; Table S1). Notably, many known targets of DR serotonin neurons (Allen Brain Atlas, 2017; Azmitia and Segal, 1978; Vertes, 1991) were not innervated by either of these subpopulations, including most of the striatum, thalamus, hypothalamus, somatosensory and motor cortex, and dorsal BNST (Table S1). Thus, the DR serotonin system contains at least two, and likely more, parallel sub-systems with distinct innervation patterns.

$DR^{Sert}\rightarrow$OFC and $DR^{Sert}\rightarrow$CeA Neurons receive biased input from specific nuclei

DR serotonin neurons as a whole receive monosynaptic inputs from diverse brain regions (Ogawa et al., 2014; Pollak Dorocic et al., 2014; Weissbourd et al., 2014). Given their parallel output organization, we next used cTRIO (cell-type-specific tracing the relationship between input and output) (Schwarz et al., 2015) to identify inputs to $DR^{Sert}\rightarrow$OFC and $DR^{Sert}\rightarrow$CeA neurons. We injected *HSV-STOP^{flox}-Flp* unilaterally into the OFC or CeA, and AAVs carrying Flp-dependent constructs expressing TVA-mCherry (TC) fusion protein and rabies glycoprotein (G) into the DR of *Sert-Cre* mice. We then injected EnvA-pseudotyped, G-deleted, GFP-expressing rabies virus (RV*dG*) into the DR. Thus, only Sert-Cre^{+} neurons that project to the OFC or CeA could become starter cells for RV*dG*-mediated transsynaptic tracing (Figure 3A).

Tph2 staining verified that starter cells were predominantly serotonin neurons (97%±2% $DR^{Sert}\rightarrow$OFC and 94%±4% $DR^{Sert}\rightarrow$CeA neurons were $Tph2^{+}$; Figure 3B). While thousands of long-range input cells were identified in each experimental group, few GFP-labeled cells were found in the two controls: those without AAV expressing G and those using wild-type instead of *Sert-Cre* mice (Figure S3A–C), confirming specificity of input tracing.

To determine the long-range presynaptic partners for $DR^{Sert}\rightarrow$OFC and $DR^{Sert}\rightarrow$CeA neurons, we counted cell numbers in each of the 35 regions of interest (Table S2) (Weissbourd et al., 2014) from serial coronal sections. While presynaptic inputs to these two

DR serotonin subpopulations originated from similar brain regions, there were striking quantitative differences. Specifically, $DR^{Sert}\rightarrow$OFC neurons received proportionally more input from lateral hypothalamus (LHy), lateral habenula (LHb), and the majority of medulla nuclei. By contrast, $DR^{Sert}\rightarrow$CeA neurons received significantly more input from CeA itself, BNST, PVH, and nucleus of the solitary tract (Figure 3C–D; Figure S3D). The marked enrichment of CeA input to $DR^{Sert}\rightarrow$CeA neurons suggests strong DR-CeA reciprocal connectivity.

In summary, $DR^{Sert}\rightarrow$OFC and $DR^{Sert}\rightarrow$CeA neurons have largely complementary collateralization patterns (Figure 2) and receive quantitatively biased input from specific brain regions (Figure 3). Next, we examined if $DR^{Sert}\rightarrow$OFC and $DR^{Sert}\rightarrow$CeA neurons also exhibit different physiological response properties and behavioral functions.

$DR^{Sert}\rightarrow$OFC and $DR^{Sert}\rightarrow$CeA Neurons Are Both Activated by Reward But Show Opposite Responses to Punishment

Previous studies showed that DR serotonin neurons, when treated as a whole, were activated during reward consumption in freely moving mice (Li et al., 2016). However, single-unit recordings in head-fixed mice revealed heterogeneous responses of DR serotonin neurons to reward and punishment (Cohen et al., 2015). Since $DR^{Sert}\rightarrow$OFC and $DR^{Sert}\rightarrow$CeA neurons receive biased presynaptic inputs from different brain regions (Figure 3), it is possible that they respond differently to reward and punishment. To test this, we combined our viral-genetic strategy with fiber photometry (Gunaydin et al., 2014) by expressing genetically encoded Ca^{2+} indicator GCaMP6m (Chen et al., 2013) in $DR^{Sert}\rightarrow$OFC or $DR^{Sert}\rightarrow$CeA neurons. To compare to projection-specific DR serotonin neurons, we also expressed Cre-dependent GCaMP6m in the DR of *Sert-Cre* mice ("DR^{Sert} group"). We implanted an optical fiber into the DR at the GCaMP6m injection site through which we delivered 490-nm excitation light to monitor the activity of different serotonin neuron groups (Figure $4A_1$–C_1), normalized by response to 405-nm control light to correct for movement artifact (Allen et al., 2017). We verified GCaMP6m expression and recording sites via *post hoc* histology (Figure $4A_2$–C_2; Figure $S4A_1$–C_1). No task-evoked photometry signals were detected in DR serotonin neurons expressing GFP instead of GCaMP6m (Figure S4D).

To record reward responses, we trained mice to lever press for a sucrose water reward in a fixed-ratio paradigm. Each lever press led to one unit of sucrose water delivered from a nearby port, and water-restricted mice were allowed free access during the recording. Consistent with a previous report (Li et al., 2016), all recordings from the DR^{Sert} group showed an activation after the onset of licking, and the evoked activity persisted during the reward consumption period (Figure $4A_3$, A_3'). The $DR^{Sert}\rightarrow$OFC and $DR^{Sert}\rightarrow$CeA groups showed similar activation pattern (Figure $4B_3$, B_3', C_3, C_3', E; Figure $S4A_5$–C_5). Interestingly, when we aligned recording with the time of lever press, we found that in some mice, and more consistently in the $DR^{Sert}\rightarrow$OFC group, serotonin neurons ramped up their activity prior to lever press (Figure $S4A_2$–C_3). Quantifications revealed significant activity increase prior to lever press in $DR^{Sert}\rightarrow$OFC neurons compared to $DR^{Sert}\rightarrow$CeA neurons (Figure 4D).

Next, we recorded responses to punishment by subjecting the same set of mice to mild electrical shocks. Remarkably, $DR^{Sert}\rightarrow$OFC and $DR^{Sert}\rightarrow$CeA neurons showed opposing responses to foot-shock. All seven mice from the $DR^{Sert}\rightarrow$OFC group showed a long-lasting reduction of Ca^{2+} signals during and after the 1-sec foot-shock (Figure $4B_4$, B_4', E). By contrast, in all eight mice from the $DR^{Sert}\rightarrow$CeA group, foot-shock induced a transient elevation of Ca^{2+} signals, followed by a small depression in a subset (Figure $4C_4$, C_4', E). The seven mice from the DR^{Sert} group showed more varied responses, including one that exhibited a biphasic response composed of a transient elevation followed by long-lasting depression (Figure $4A_4$, A_4').

These data indicate that $DR^{Sert}\rightarrow$OFC and $DR^{Sert}\rightarrow$CeA neurons respond similarly to reward, differently while anticipating an action that leads to reward, and oppositely to punishment. These findings suggest that previously described heterogeneous physiological responses of DR serotonin neurons to reward and punishment (Cohen et al., 2015) could result from recordings from projection-specific subpopulations.

Both $DR^{Sert}\rightarrow$OFC and $DR^{Sert}\rightarrow$CeA Neurons Suppress Locomotion

To investigate the behavioral functions of $DR^{Sert}\rightarrow$OFC and $DR^{Sert}\rightarrow$CeA neurons, we employed two complementary approaches. In a gain-of-function approach, we expressed the hM3Dq chemogenetic activator (Armbruster et al., 2007) in $DR^{Sert}\rightarrow$OFC or $DR^{Sert}\rightarrow$CeA neurons by unilaterally injecting *AAV_{retro}-FLEx-Flp* into the OFC or CeA of *Sert-Cre* mice, and Flp-dependent hM3Dq (Beier et al., 2017) into the DR in the experimental group. In the two control groups for each experimental group, we replaced either hM3Dq with GFP or *Sert-Cre* with wild-type mice (Figure $5A_1$, B_1). *Post hoc* histology confirmed that hM3Dq expression was Cre-dependent and cells' locations were consistent with previous results (Figure $5A_2$, B_2). Whole-cell recordings of hM3Dq-expressing DR *Sert-Cre^+* neurons in brain slices validated that application of Clozapine N-oxide (CNO) enhanced the firing rate of hM3Dq-expressing but not control serotonin neurons (Figure S5A–C). In a loss-of-function approach, we conditionally knocked-out *Tph2* from $DR^{Sert}\rightarrow$OFC or $DR^{Sert}\rightarrow$CeA neurons by bilaterally injecting *AAV_{retro}-Cre-2A-GFP* into the projection site of *$Tph2^{flox/flox}$* mice (Wu et al., 2012) 17 days prior to the onset of behavioral tests. As a control, we injected *AAV_{retro}-GFP* instead (Figure $5C_1$, D_1). Staining of *$Tph2^{flox/flox}$* mice showed a lack of Tph2 protein in GFP^+ DR neurons (Figure $5C_2$, D_2) and significantly reduced terminal serotonin levels (Figure S5C–D), confirming the effectiveness of viral-mediated knockout. Although the vast majority of $Tph2^+$ neurons that project to OFC and CeA were from DR, a small fraction were from median raphe (Figure S5E); thus median raphe serotonin neurons may have a small contribution to the loss-of-function phenotypes described below.

We subjected the same sets of mice to a series of behavioral paradigms known to engage the DR serotonin system in a fixed sequence (STAR Methods). We first quantified locomotion in the open field and found that chemogenetic activation of both $DR^{Sert}\rightarrow$OFC and $DR^{Sert}\rightarrow$CeA neurons significantly decreased locomotion compared with controls (Figure 5E, G). Conversely, Tph2 depletion from $DR^{Sert}\rightarrow$CeA neurons significantly increased locomotion over controls, suggesting that serotonin is responsible for the locomotion

suppression promoted by DR^{Sert}→CeA neurons (Figure 5H). However, Tph2 depletion from DR^{Sert}→OFC neurons did not affect locomotion (Figure 5F); one possibility is that the effect caused by activating this subpopulation involves glutamate, as most DR^{Sert}→OFC neurons were $Vglut3^{+}$ (Figure 1G). Indeed, by combining channelrhodopsin-assisted circuit mapping, local field potential recording in OFC slices, and pharmacology, we found that DR^{Sert}→OFC fibers co-released serotonin and glutamate to modulate OFC network activity (Figure S6).

DR^{Sert}→CeA but not DR^{Sert}→OFC Neurons Promote Anxiety-like Behavior

Next, we tested the effects of manipulating DR^{Sert}→OFC and DR^{Sert}→CeA neurons on anxiety-like behavior. Excessive avoidance of the center in the open field or the open arms of the elevated plus maze (EPM) are widely used as indications of anxiety-like behavior. We found that activation of DR^{Sert}→OFC neurons did not affect center entry or center time in the open field, or open-arm entry or time in open arms of the EPM (Figure 6A, E). However, Tph2 depletion from DR^{Sert}→OFC neurons caused a significant decrease in center time and center entry compared with controls (Figure 6B), as well as a significant decrease in open-arm time in the EPM (Figure 6F). These data suggest that serotonin release in the DR→OFC projection has an anxiolytic effect.

By contrast, activation of DR^{Sert}→CeA neurons promoted anxiety-like behavior, causing significantly decreased center entry and center time in the open field (Figure 6C) and activation significantly decreased open arm entry and open arm time (Figure 6G) compared to all controls except one case. Conversely, Tph2 depletion from DR^{Sert}→CeA neurons appeared anxiolytic, causing a significant increase in center entry in the open field (Figure 6D) and open arm time in EPM (Figure 6H). Taken together, these data suggest that DR^{Sert}→CeA neurons are anxiogenic.

We also used auditory fear conditioning to test the effect of manipulating DR^{Sert}→CeA and DR^{Sert}→OFC neurons. Neither activation nor Tph2 depletion of DR^{Sert}➔OFC neurons affected fear learning and memory recall (Figure S7A, B, E, F). By contrast, activation of DR^{Sert}→CeA neurons significantly increased overall freezing time to the conditioned tone in fear learning and memory recall (Figure S7C, D). However, fear learning and memory were not affected by Tph2 depletion in DR^{Sert}→CeA neurons (Figure S7G, H), suggesting that other pathways may compensate for the loss of DR^{Sert}→CeA activity in fear learning and memory.

DR^{Sert}→OFC but not DR^{Sert}→CeA Neurons Enhance Active Coping

Finally, we asked whether DR^{Sert}→CeA and DR^{Sert}→OFC neurons could modulate coping behavior in a 2-day forced-swim test. Immobility and struggle (escape behavior) in the forced-swim test are often used as indications of passive and active coping in the face of challenge, respectively. During chemogenetic experiments, CNO was administrated only before the day-2 test. Whereas chemogenetic activation of DR^{Sert}→CeA neurons did not affect immobility (Figure 7C), Tph2 depletion significantly reduced immobility during the forced-swim test (Figure 7D); this suggests that DR^{Sert}→CeA neurons inhibit escape

behavior, although we cannot rule out this being a secondary effect on movement (Figure 5H).

Remarkably, activation of $DR^{Sert}\rightarrow$OFC neurons significantly enhanced escape behavior (decreased immobility) after CNO application on the day-2 test (Figure 7A, Figure S7I). Moreover, *Tph2* deletion from $DR^{Sert}\rightarrow$OFC neurons increased immobility (Figure 7B). Thus, both gain- and loss-of-function experiments indicate that $DR^{Sert}\rightarrow$OFC neurons promote escape behavior in the forced-swim test. Taken together, these data suggest that activation of $DR^{Sert}\rightarrow$OFC (but not $DR^{Sert}\rightarrow$CeA) neurons promotes active coping in the face of challenge, and that serotonin release is necessary for this effect.

Discussion

DR serotonin neurons project broadly and modulate diverse functions. It has been unclear how they are anatomically and functionally organized. Here we provide evidence for the existence of parallel sub-systems that differ in input and output connectivity, physiological response properties, and behavioral functions.

Anatomical Organization of the DR Serotonin System

Previous anterograde and retrograde tracing suggested that the DR is organized along both the anterior-posterior (Abrams et al., 2004; Commons, 2015) and dorsal-ventral axes (Lowry et al., 2005; Muzerelle et al., 2016), and that individual DR neurons can send collaterals to two or more separate brain regions (Gagnon and Parent, 2014). However, different studies have not fully agreed upon the details of the topography due to technical limitations. For anterograde tracing, the resolution is limited by the spread of injected dyes or the genetic access to subtypes of DR serotonin neurons. For retrograde labeling, each study usually focused on a small subset of targets. Collateralization patterns are poorly understood because most data were collected by injecting two retrograde tracers into two pre-specified brain regions and observing double- labeled DR serotonin neurons, which provides limited insight into the overall extent of the collateralization.

Our retrograde tracing combined with image registration provides a more comprehensive view of the spatial organization of DR serotonergic projections in the mouse (Figure 1). With the exception of ENT-projecting DR serotonin neurons, which tended to localize to caudal DR, we did not find a prominent anterior-posterior topographic. We did find that ventral and dorsal serotonin neurons preferentially innervated cortical and subcortical targets, respectively, confirming and extending previous reports (Lowry et al., 2005; Muzerelle et al., 2016; Prouty et al., 2017). We further uncovered a strong correlation between cortical projections and Vglut3 co-expression in DR serotonin neurons, and demonstrated that OFC-projecting serotonin neurons co-release glutamate to regulate cortical activity (Figure S6). An interesting speculation is that glutamate co-release in cortex allows the DR serotonin system to regulate cortical circuits on a more rapid time scale via ionotropic glutamate receptors, whereas release of serotonin alone in subcortical circuits primarily serves a slower modulatory function via metabotropic receptors. Indeed, ionotrophic serotonin receptors are preferentially expressed in cortical and hippocampal interneurons (Barnes and Sharp, 1999).

Viral-genetic labeling in combination with whole-mount imaging revealed for the first time whole-brain collateralization patterns of projection-defined DR serotonin neurons, showing that DR^{Sert}→OFC and DR^{Sert}→CeA axons innervate largely complementary targets (Figure 2; Figure S2; Movies S2, S3). These analyses further indicate that the collateralization of individual DR serotonin neurons can be extremely broad (e.g., DR^{Sert}→OFC neurons also innervate OB anteriorally and ENT posteriorally) yet highly specific (e.g., DR^{Sert}→OFC neurons innervate cortical amygdala but avoid the nearby basolateral amygdala). These collateralization data comprise a map indicating which brain targets are likely coordinately or differentially modulated by serotonin.

cTRIO analyses further revealed that DR^{Sert}→OFC and DR^{Sert}→CeA neurons receive biased input from specific brain regions (Figure 3). Thus, the input-output architecture of the DR serotonin system differs from that of the locus coeruleus norepinephrine system with more homogeneous input and output (Schwarz et al., 2015), and resembles more closely those of the midbrain dopamine systems (Beier et al., 2015; Lerner et al., 2015), with biased input and segregated output. We want to emphasize that each sub-system we characterized may still be heterogeneous in their composition. For example, DR^{Sert}→OB neurons may be better described by a two-cluster model (STAR Method). Future systematic analyses utilizing the methods employed here, supplemented by high-resolution tracing of the axonal arborizations of individual serotonin neurons, will provide a more complete understanding of how the ~9,000 DR serotonin neurons differentially innervate target fields to modulate diverse physiological functions.

Distinct Functions of the DR^{Sert}→OFC and DR^{Sert}→CeA Sub-systems

We used chemogenetic activation as a gain-of-function and Tph2 depletion as a loss-of-function approach to functionally dissect projection-specific DR serotonin neurons. Because gain-of-function experiments alone may not reflect physiological functions of the system under manipulations, we consider our conclusions stronger if loss- and gain-of-function experiments generate opposite effects. There are advantages to using Tph2 depletion instead of chemogenetic silencing as a loss-of-function approach. First, chemogenetic silencing requires a higher CNO concentration than does chemogenetic activation; as the active component of CNO may be clozapine (Gomez et al., 2017), which engages several serotonin receptors at high concentrations (Meltzer, 1994), this strategy may ectopically affect serotonin-related behavior. Second, since a large fraction of DR serotonin neurons likely co-releases glutamate, Tph2 depletion specifically addresses the function of serotonin in these neurons. A caveat is that this manipulation is irreversible, and compensatory changes may occur in the circuit during the time between AAV_{retro}-*Cre* injection and behavioral testing; thus, this loss-of-function strategy may not reveal the full function of serotonin release.

The DR serotonin system has been consistently shown to negatively regulate locomotion (Correia et al., 2017; Teissier et al., 2015; Whitney et al., 2016). Our data (Figure 5) suggest that the inhibitory effect of DR serotonin neurons on locomotion is at least partly mediated by serotonin release from DR^{Sert}→CeA neurons. Glutamate released from DR^{Sert}→OFC neurons may also contribute to this effect.

The role of serotonin in anxiety-like behavior in the cortex has been extensively studied with pharmacological and genetic manipulations of serotonin receptors (Albert et al., 2014). However, given the opposing roles of different serotonin receptors and their complex expression patterns in excitatory and inhibitory cortical neurons, it is difficult to predict the effect of cortical serotonin release on anxiety. We found that while chemogenetic activation of $DR^{Sert}\rightarrow$OFC neurons did not significantly affect anxiety-like behavior, conditional Tph2 depletion in these neurons enhanced anxiety-like behavior (Figure 6). Since $DR^{Sert}\rightarrow$OFC neurons mostly co-express Vglut3 (Figure 1) and can co-release glutamate (Figure S6), one interpretation is that activation of $DR^{Sert}\rightarrow$OFC neurons results in release of both glutamate and serotonin that have opposing effects on anxiety-like behavior. When serotonin is selectively removed from this pathway, anxiety-like behaviors were promoted, suggesting that cortical serotonin release suppresses anxiety. In contrast, both gain- and loss-of-function experiments indicated that $DR^{Sert}\rightarrow$CeA neurons promote anxiety-like behavior (Figure 6 and Figure S7). $DR^{Sert}\rightarrow$CeA neurons collateralize to other amygdala nuclei, BNST, and PVH (Figure 2), all of which have been implicated as anxiety-related regions (Calhoon and Tye, 2015). Moreover, cTRIO analysis revealed that CeA and BNST provided particularly strong input to $DR^{Sert}\rightarrow$CeA neurons compared to $DR^{Sert}\rightarrow$OFC neurons (Figure 3). Thus, our data demonstrate that $DR^{Sert}\rightarrow$CeA neurons promote anxiety-like behavior, likely involving reciprocal connections between the DR and CeA/BNST.

A recent large-scale meta-analysis provided strong evidence for the efficacy of selective serotonin reuptake inhibitors in treating depression (Cipriani et al., 2018). Immobility in the forced-swim test represents a passive coping strategy in the face of challenge and is often used to indicate a depression-like state in rodent models (Petit-Demouliere et al., 2005). Chemogenetic activation of DR serotonin neurons has recently been reported to reduce immobility in the forced-swim test (Teissier et al., 2015). Both our gain- and loss-of-function manipulations in the forced-swim test suggest that $DR^{Sert}\rightarrow$OFC neurons, but not $DR^{Sert}\rightarrow$CeA neurons, mediate this effect (Figure 7). Optogenetic activation of prefrontal cortical neuron terminals in the DR has previously been shown to promote active coping (Warden et al., 2012). Furthermore, frontal cortex inputs to the DR preferentially synapse onto serotonin neurons that are localize in the ventral DR (Weissbourd et al., 2014), where $DR^{Sert}\rightarrow$OFC neurons also localize (Figure 1). Thus, $DR^{Sert}\rightarrow$OFC neurons and frontal cortex$\rightarrow DR^{Sert}$ neurons may constitute a reciprocal loop to promote active coping in the face of challenge.

Technical difficulties make obtaining fiber photometry data during the above behaviors modulated by $DR^{Sert}\rightarrow$OFC and $DR^{Sert}\rightarrow$CeA neurons difficult. Nevertheless, the differential response properties of $DR^{Sert}\rightarrow$OFC and $DR^{Sert}\rightarrow$CeA neurons in the context of reward and punishment are consistent with their behavioral functions, and functions described by previous studies. For example, $DR^{Sert}\rightarrow$OFC neurons appear to encode positive valence; they are also activated in anticipation of an action that leads to reward. We speculate that both properties may contribute to a behavioral role of promoting active coping in the face of challenge (Figure 7) and waiting for delayed reward (Miyazaki et al., 2012). Their inhibition by punishment could play a role in depression-like states induced by aversive stimuli. On the other hand, activation of $DR^{Sert}\rightarrow$CeA neurons by punishment is

consistent with a behavioral function of promoting anxiety, a brain state often equated to anticipation of future punishment.

In conclusion, our behavioral analyses demonstrate that anatomically-segregated DR subsystems have distinct, and sometimes even opposing, functions (Figure 7E). Thus, DR serotonin neurons should no longer be viewed as a monolithic population. We have provided means to further dissect the complexity of the DR serotonin system; such an endeavor will advance our understanding of neuromodulation in health and aid our development of effective therapies for brain disorders such as anxiety and depression.

STAR METHODS

CONTACT FOR REAGENT AND RESOURCE SHARING

Further information and requests for resources and reagents should be directed to and will be fulfilled by the Lead Contact, Liqun Luo (lluo@stanford.edu).

EXPERIMENTAL MODEL AND SUBJECT DETAILS

Animals—All procedures followed animal care and biosafety guidelines approved by Stanford University's Administrative Panel on Laboratory Animal Care and Administrative Panel of Biosafety in accordance with NIH guidelines. For anatomical experiments (Figures 1–3), male and female mice aged 8–20 weeks on a CD1 and C57BL/6J mixed background were used. The *Ai14* tdTomato Cre reporter mice (JAX Strain 7914), *Vglut3-Cre* (also known as *Slc18a8-Cre*; JAX Strain 18147), and *Sert-Cre* (MMRRC, Stock #017260-UCD) were used where indicated. For all other experiments (Figures 4–7), male mice aged 8–12 weeks on the C57BL/6J background were used when the experiments started; these mice had no prior procedure except for viral injection or/and fiber implantation. Animals were randomly assigned to experimental groups. $Tph2^{flox/flox}$ was obtained from Qi Wu (Wu et al., 2012). All mice used in fiber photometry recording were group housed with littermates, and they were trained and tested in the lever-pressing experiments before the foot shock experiment. All male mice used in gain- and loss-of-function behavioral experiments were test naïve for individual behavioral paradigms, and were individually housed with one female partner. Mice were housed in plastic cages with disposable bedding on a 12 hours light/dark cycle with food and water available *ad libitum*, except when placed on water restriction. Experiments were done during the light phase.

METHOD DETAILS

Stereotaxic Surgeries—Mice were anesthetized either with ketamine/dexmedetomidine mixture (Figure 1 and Figure 3) or 1.5%–2.0% isoflurane (Figure 2 and Figure 4–7) and placed in a stereotaxic apparatus (Kopf Instruments). For virus injection, the following coordinates (in mm) were used: +4.0 AP, 0.75 ML, –1.5 DV for OB; +2.6 AP, 1.7 ML, –1.7 DV for OFC; + 1.2 AP, 2.8 ML, –4.5 DV for PIR; –3.3 AP, 4.5 ML, –4.5 DV for ENT; 0.2 AP, 0.6 ML, –4.9 DV for PVH; –1.05 AP, 2.86 ML, –4.55 DV for CeA; –1.4 AP, 0.4 ML, –2.6 DV for LHb; –2.3 AP, 2.6 ML, - 2.7 DV for dLGN; –4.3AP, 1.10 ML, –2.85 DV for DR, with 20° ML angle. (AP is relative to bregma; DV is relative to the brain surface when AP is

–1.0). After surgery, mice recovered on a heated pad until ambulatory and then returned to their homecage.

Viruses—Viruses with the following volumes and titers were injected and the injection time lines were listed in Table S4:

HSV-hEF1a-cre, 2×10^9 infectious units/ml;

OB, 500 nl; OFC, 750 nl; PIR, 500nl; ENT, 500 nl; PVH, 300 nl; CeA, 300 nl; LHb, 300 nl; dLGN, 500 nl.

HSV-hEF1a-LS1L-FLPo, 5×10^9 infectious units/ml;

OFC, 750 nl; CeA, 300 nl.

eGFP-expressing G-deleted Rabies Virus, 1×10^9 gc/ml;

OB, 500 nl; OFC, 750 nl; PIR, 500 nl; ENT, 500 nl; PVH, 300 nl; CeA, 300 nl; LHb, 300 nl; dLGN, 500 nl.

EnvA-pseudotyped, eGFP-expressing G-deleted Rabies (RV*dG*), 1×10^9 gc/ml;

DR, 500 nl.

AAV_{retro}-*CAG-FLEx*^{loxP}-*Flp*, 6.9×10^{12} gc/ml;

OFC, 750 nl; CeA, 300 nl.

AAV8-hSyn1-FLEx^{FRT}-*mGFP*, 2.9×10^{13} gc/ml;

DR, 500 nl.

AAV5-CAG-FLEx^{FRT}-*TC*, 2.6×10^{12} gc/ml, *AAV8-CAG-FLEx*^{FRT}-*G*, 1.3×10^{12} gc/ml;

DR, 500 nl;

AAV1-hEF1a- FLEx^{loxP}-*GCaMP6m*, 1×10^{13} gc/ml;

DR, 500 nl;

AAV8-CAG- FLEx^{FRT}-*GCaMP6m*, 1.8×10^{13} gc/ml;

DR, 500 nl;

AAV8-hsyn1-FLEx^{FRT}-*hM3Dq-mCherry*, 6.2×10^{12} gc/ml;

DR, 500 nl;

AAV_{retro}-*CMV-Cre-2A-eGFP*, 8.7×10^{12} gc/ml;

OFC, 750 nl; CeA, 300nl.

AAV_{DJ}-*EF1a-DIO-hM3D(Gq)-mCherry*, 4.83×10^{13} gc/ml;

DR, 750 nl;

AAV_{DJ}-*EF1-DIO-hChR2(H134R)-EYFP*, 5.27×10^{13} gc/ml

DR, 500 nl.

Note that we used three different viruses for retrograde labeling: HSV, AAV_{retro}, and RV*dG*. Table S4 listed the number of infected DR serotonin neurons via output sites from these three viruses in various experiments utilizing these viruses, as well as times from viral injections to data collection. In general AAV_{retro} yields higher efficiency, which is the reason why we switched to AAV_{retro} after it was introduced in 2016.

Histology and Imaging—Animals were perfused transcardially with phosphate buffered saline (PBS) followed by 4% paraformaldehyde (PFA). Brains were dissected, post-fixed in 4% PFA for 12–24 hours in 4 ºC, then placed in 30% sucrose for 24–48 hours. They were then embedded in Optimum Cutting Temperature (OCT, Tissue Tek) and stored at –80ºC until sectioning. For the antibody staining in Figure 1, 50-μm sections containing DR were collected onto Superfrost Plus slides to maintain the anterior to posterior sequence. All working solutions listed below included 0.2% NaN_3 to prevent microbial growth. Slides were then washed 3×10 min in PBS and pretreated overnight with 0.5 mM SDS at 37ºC. Slides were then blocked for 4 hours at room temperature in 10% normal donkey serum (NDS) in PBS with 0.3% Triton-X100 (PBST), followed by incubation in primary antibody (Novus, rabbit anti-Tph2) diluted 1:1000 in 5% NDS in PBST for 24 hours at RT. After 3×10 min washes in PBS, secondary antibody was applied for 6 hours at room temperature (donkey anti-rabbit, Alexa-647 or Alexa-488, Jackson ImmunoResearch), followed by 3×10 min washes in PBST. Slides were then stained for NeuroTrace Blue (NTB, Invitrogen). For NTB staining, slides were washed 1×5 min in PBS, 2×10 min in PBST, incubated for 2–3 hours at room temperature in (1:500) NTB in PBST, washed 1×20 min with PBST, and 1×5 min with PBS. Sections were additionally stained with DAPI (1:10,000 of 5 mg/mL, Sigma-Aldrich) in PBS for 10–15 min and washed once more with PBS. Slides were mounted and coversliped with Fluorogel (Electron Microscopy Sciences). After that, the slides were then imaged using a Zeiss 780 confocal microscope, and images were processed using NIH ImageJ software. After that, whole slides were then imaged with a 5x objective using a Leica Ariol slide scanner with the SL200 slide loader.

For long-range tracing analysis in cTRIO experiments (Figure 3), consecutive 50-μm coronal sections covering the whole brain (with the exception of sections including the DR) were collected and NTB stained as described above. For DR-containing slices in Figure 3–7, staining was applied to floating sections. Primary antibodies (Novus, rabbit anti-Tph2, 1:1000; Rockland, rabbit anti-RFP, 1:1000; Abcam, goat anti-Tph2, 1:500; Aves Labs Inc., anti-GFP, 1:2000) were applied for 48 hours and secondary antibodies for 12 hours at 4ºC.

For serotonin staining, animals were perfused transcardially with modified aCSF containing (in mM): 225 sucrose, 119 NaCl, 2.5 KCL, 1 NaH_2PO4, 4.9 $MgCl_2$, 0.1 $CaCl_2$, 26.2 $NaHCO_3$, 1.25 glucose, 3 kynurenic acid, and 1 Na-ascorbate (all chemicals were from Sigma, St Louis, MO, USA), followed by 4% paraformaldehyde (PFA). Brains were dissected, post-fixed in 4% PFA for 12 hours at 4 ºC, and placed in 30% sucrose for 24–48 hours at 4 ºC. They were then embedded in Optimum Cutting Temperature (OCT, Tissue Tek) and stored at in the –80ºC freezer until sectioning. 30-μm sections containing OFC and CeA were collected every three slices as floating sections. And then they were blocked for 4 hours at room temperature in 10% normal donkey serum (NDS) in PBS with 0.3% Triton-X100 (PBST). Primary antibody (ImmunoStar, rabbit anti-5HT, 20080) was diluted 1:5000

in 5% NDS in PBST, and incubated for 48 hours at 4 ºC and secondary antibodies 12 hours at 4ºC.

2D Registration—For 2D registration (Figure 1 and S1), whole-slide images of scanned slides were imported into custom Matlab software to segment images into individual brain sections based on the NTB stain. To accelerate processing, the full resolution images (xy-resolution =1.29 μm/pixel) were initially down-sampled by a factor of 32 in both x- and y-dimensions. Segmentation included the application of a mask fit to the edge of each section to remove all image features outside the section. Background subtraction and contrast enhancement of the NTB channel were then applied. The processed NTB images for each section were then serially analyzed using a combination of automated and manual methods. To estimate the sectioning angle differences between individual samples and the Allen reference brain (Allen Institute for Brain Science, 2015, http://brain-map.org/api/index.html), we assumed a parallel sectioning angle for each brain. To generate a standard atlas accounting for different sectioning angles, the atlas was rotated, re-sectioned into coronal slices, and slices were re-indexed in order. The histological sequence of each sample was compared to the newly generated re-sectioned atlas slices. Every third slice of the experimental brain was automatically selected for quantitative evaluation of the cutting angle difference (severely damaged slices were skipped). Images from each group were first introduced to the same coordinates using a similarity transformation estimated by the Umeyama method based on contour point correspondence generated by Shape Context. Slices were further rescaled in the horizontal and vertical directions to accommodate the global deformation. Features identified by Histogram of Oriented Gradients (HOG) were then extracted from both images, and the L2 norm of HOG difference was used as the similarity metric. The difference between two images is measured as a scalar, which is the summation of the HOG difference over all blocks. Matching slice index differences of half brains were used to determine the cutting angle. Matching slice indices were then interpolated linearly to identify the best matching atlas section for each sample slice in the experimental brain. All the experimental slices were registered non-rigidly to their computed corresponding slice in the optimally rotated atlas to build a pixel-wise mapping from the 2D slice sequence to the reference volume. We augmented the Markov random field (MRF) approach to model brain tissue coherency. We made further improvements based on the data-specific properties of our experimental dataset, including segmenting the aqueduct with a convolutional neural network and locally warping it with a thin plate spline (TPS). For a more detailed description of this procedure see Xiong et al. (2018).

3D Reconstruction and Clustering of DR Neurons—To construct the volume presenting DR serotonin neurons, slices containing the Tph2-positive neurons from four animals were registered to Allen's reference atlas (4698 ± 376.6 per brain, caudal DR was excluded). The line connecting the highest and lowest points of the aqueduct was defined as the midline, with a "zero" value along the medial-lateral axis. To reflect the bilateral symmetry of the DR serotonin system, mirror images were created for each cell across the midline plane (Figure S1A). All the cells' 2D positions were determined automatically by custom Matlab program employing k-means, followed by 3D registration. DBSCAN was performed to cluster the combined data and establish a 3D surface of the DR serotonin

system that covered ~97% of Tph2-positive neurons using custom software. Delaunay Triangulation was then performed on the clusters outputted from DBSCAN to define the boundaries. Catmull Clark subdivision was then applied to the boundary to finalize the shape of 3D clusters.

For each brain with specific retrograde injections and Tph2/Vglut3 dual-labeled neurons, the 2D positions of the neurons were determined manually and registered to the same reference atlas, allowing cross-comparison of the data from the DR of different brains. DBSCAN was performed to cluster individual groups and establish each 3D surface. To find a good pair of parameters, we explored the entire parameter space and each pair's respective resulting cluster boundaries by generating 10,000 pairs of parameters for each set of data. We then extracted three features (number of clusters, average density, and coverage) to evaluate the groups resulting from each parameter selection. We plotted the relationship between average density and coverage of all the pairs from the ten datasets that generate a >60% coverage of the total cells. We found that, for nine out of ten datasets, one cluster had the same expressive power as multiple clusters and the only sub-system that might be better described as two clusters is $DR^{Sert}\rightarrow$OB. Thus we decide to choose one cluster representation for each dataset, since the main purpose of this visualization attempt is to show the spatial distribution proportion of each projection defined serotonin neurons. We also noted that six out of ten of these datasets have a "knee" around 85% coverage that describes the best point in terms of a tradeoff between coverage and density. We therefore used the pair of parameters that have the largest average density when the coverage is around 85%. MinPints, minimum number of points required to form a dense region. Eps, epsilon.

	MinPints	Eps	Cluster #	Density	Coverage
$DR^{Sert}\rightarrow$PVH	9	165	1	0.0018	85.96%
$DR^{Sert}\rightarrow$CeA	11	177	1	0.0012	82.97%
$DR^{Sert}\rightarrow$LHb	8	183	1	0.0010	79.91%
$DR^{Sert}\rightarrow$dLGN	12	201	1	0.0010	87.64%
$DR^{Sert}\rightarrow$PIR	14	157	1	0.0030	82.08%
$DR^{Sert}\rightarrow$OFC	10	130	1	0.0035	83.46%
$DR^{Sert}\rightarrow$ENT	11	193	1	0.0015	81.24%
$DR^{Sert}\rightarrow$OB	8	176	1	0.0015	86.03%
$DR^{Sert}\rightarrow$OB	14	195	2	0.0020	80.15%
$DR^{Sert}\rightarrow$subcortical area	16	149	1	0.0023	81.93%
$DR^{Sert}\rightarrow$anterior cortical area	13	150	1	0.0023	82.17%

Further processing followed the procedures described above. To test whether the two-component model we proposed based on the raw data can hold regardless of the parameter choice, we examined the subcortical and cortical groupings that resulted from the randomly chosen 10,000 pairs of parameters. We sampled a random cortical grouping with a random subcortical grouping 10,000 times and calculated the respective overlap percentage. To ensure each randomly sampled grouping were plausible, we only used groupings that had

more than 60 percent coverage. We found that the mean overlap percentage was 22.25% ± 4.01% (mean ± standard deviation). Additionally there exists no grouping of subcortical and cortical that has more than 30% overlap. Thus, we conclude that the positions of serotonin neurons with subcortical and cortical projections are largely separate regardless of the various boundaries that are possible.

Cell Density and Line Density—Cell density at location D, denoted as $D(x, y, z)$, is a function that calculates cell numbers located in a 3D coordinate system defined by x (axis M→L), y (axis D→V), and z (axis A→P). Define $N(x_0, y_0, z_0)$ to be the number of cells located in space defined by $x \leq x_0, y \leq y_0, z \leq z_0$.

$$D(x = x_0, y = y_0, z = z_0) = \frac{N(x_0 + \Delta x, y_0 + \Delta y, z_0 + \Delta z) - N(x_0, y_0, z_0)}{\Delta x \times \Delta y \times \Delta z}$$

Cell linear density along y at location y_0 is defined as

$$D_y(y = y_0) = \frac{N(y_0 + \Delta y) - N(y_0)}{\Delta y}$$

$N(y_0)$ refers to the number of cells at location defined by $y \leq y_0$, i.e. ventral to the brain surface at y_0μm.

iDISCO-based Whole-Brain Axon Tracing—Brains were perfused, dissected, and processed according to the iDISCO+ pipeline as previously described (Renier et al., 2016). Whole brains were processed in 5-ml volumes, labeled with a 1:2000 dilution of anti-GFP antibody (Aves, GFP-1020) for 10 days and secondary Alexafluor 647 (Jackson Immunoresearch) for 7 days. Images were collected with a LaVision Lightsheet UltramicroscopeII at 0.8X magnification using 640 nm and 488 nm imaging lasers and a z-step size of 3 μm. The working distance of the microscope allowed visualization of the right hemisphere of each brain in the sagittal plane with an approximate imaging depth of 6 mm. The image stack of GFP^+ axons in the 640-nm channel was first processed with a series of high-pass filters to reduce background noise and striping artifacts generated by shadows from the lightsheet. A 2D pixel classifier was trained in Ilastik using 2–5 images from each of 8 brains. Autofluorescent fiber tracts were separated from labeled axons with a second pixel classifier. Contiguous 3D objects were classified in Matlab according to volume, solidity, orientation, intensity, and proximity to remove artifacts with similar properties. The image stack of autofluorescence in the 488 nm channel was aligned to a reference brain generated by serial two photon tomography that was co-registered to the Allen Institute's Common Coordinate Framework (CCF) (Zeng, 2018). Subsequently, the processed stack of axons was transformed to the same coordinates. Registration and transformation were performed using the Elastix toolbox (Klein et al., 2010; Shamonin et al., 2013). Voxels classified as axons were equally thresholded in all brains and counted by regions as described in the 2017 CCF. Within the Allen's hierarchy of brain areas, regions distinguished solely by layers or anatomical location were collapsed into their "parent" region (e.g., Layers 1–6 of both dorsal and ventral anterior cingulate area are labeled as

"anterior cingulate area"). These decisions were made prior to analysis and were agreed upon by four separate anatomical experts. Reported values of axonal labeling density for individual brain regions were normalized both to the volume of the region itself and the total labeling density for that sample to eliminate variability due to injection volume. Regions are sorted by divided based on comparing mean intensity between groups, and values are then sorted by their second principal component. Fiji and Imaris software were used to generate images.

cTRIO Experiments—Mice were anaesthetized with 65 mg/kg ketamine and 13 mg/kg xylazine (Lloid Laboratories) via intra-peritoneal injection and injected with 500 nl of a 1:1 mixture of AAV8 CAG-FLExFRT-G and AAV5 CAG-FLExFRT-TC into the DR, and also injected with either 750 nl HSV-STOPflox-Flp into ipsilateral OFC or 300 nl into ipsilateral CeA using coordinates described above. After recovery, mice were housed in a BSL2 facility. Two weeks later, 500 nl RVdG was injected into the DR using the procedure described above. After recovery, mice were housed in a BSL2 facility for 5 days before euthanasia.

Cell counting was performed manually using Fiji. For quantifications of subregions, boundaries were based on the Allen Institute's reference atlas (Lein et al., 2007) with consultation of Franklin and Paxinos (2013). The infralimbic cortex and medulla are as defined in the Allen atlas; for medulla, sections anterior to the appearance of the DR were omitted due to possible local background (Figure S3). For counts of thalamic subregions, we were conservative while counting sections that border midbrain nuclei, so our counts may underestimate posterior thalamic subregions. We did not adjust for the possibility of double counting cells from consecutive sections, which would result in overestimates/tion, the extent of which would depend on the size of the cells in the regions quantified.

Fiber Photometry—For virus injection and fiber optic cannula implantation, mice were anesthetized with 1.5%–2.0% isoflurane. For DR^{Sert} group, *AAV1-hEF1a- FLEx^{loxP}*-GCaMP6m was injected into the DR (500nl). For DR^{Sert}→OFC and DR^{Sert}→CeA group, AAV_{retro}-CAG-$FLEx^{loxP}$-Flp was injected into the OFC (750nl) or the CeA (300 nl) bilaterally, followed by AAV8-CAG-$FLEx^{FRT}$-GCaMP6 injection into the DR (500 nl). For fiber photometry experiments, a fiber optic cannula was implanted over the DR through the same hole used during the virus injection. To reduce autofluorescent artifacts and maximize light collection, cannulae (special order from Doric Lenses) were fabricated using 0.48 NA 400 μm BFH48–400 fibers, non-fluorescent epoxy and metal 2.5 mm ferrules. Cannulae were fixed to the skull using dental cement (Parkell, C&B metabond). After surgery, mice recovered on a heated pad until ambulatory and then returned to their homecage. Each groups comprised two cohorts.

Fiber photometry was performed using modulated 405 nm and 490 nm LEDs (Thorlab, M405F1 and M490F3). The light path was coupled to a 0.53-NA, 400-μm optical fiber patch cord, which was then coupled to the fiber implant in each mouse. Behavioral data from the operant system was synchronized to the fluorescence data using a TTL pulse at the start of each session. Signals were digitized using a digital signal acquisition board, demultiplexed using a software lock-in amplifier, and then low-pass filtered to 30 Hz before saving to disk

at 381 samples/s. At the start of each recording session, fluorescence values in the 490-nm and 405-nm channels were approximately matched to ensure accurate fitting and subtraction during analysis. Three weeks after viral injection and fiber implantation, and before recording during behavior, mice were screened for high GCaMP expression. For the lever-pressing experiments, GCaMP-expressing mice were trained to drink in the operant box after lever pressing. After reaching proficiency, mice were tested with the following protocol: after 48 hours of water-restriction, mice were allowed to lever press to obtain 5% sucrose reinforcements for at least 20 trials. The fluorescence signals, reinforcements, and licks were recorded throughout the session. For the foot-shock experiments, GCaMP-expressing mice were first habituated to the shock box for 15 minutes. 24 hours later, mice were exposed to 12 delivered 0.5-mA, 1 s electric shocks in random interval in a 40min session. The start of each shock was marked by a TTL pulse.

Fiber photometry data were analyzed in MATLAB. Each channel was loaded and resampled to 3.81 Hz. The 405-nm channel was scaled to the 490-nm channel using a least-squares fit, and then $\Delta F(t)/F0 = (F490(t) - \text{scaledF405}(t)) / \text{scaledF405}(t)$ was computed and smoothed with a 1.9 s moving average filter. Finally, the median $\Delta F(t)/F0$ from the 5-min baseline period (prior to licking or stimulus delivery in each experiment) was subtracted from the entire trace.

Patch-clamp Whole-Cell Recording—To determine how hM3Dq expressing and non-expressing DR serotonin neurons respond to CNO application, we injected AAV_{DJ}-EF1a-DIO-hM3D(Gq)-mCherry into the DR of 8-week male Sert-Cre mice. Three weeks later, acute coronal sections encompassing the DR were sliced for electrophysiological experiments according to previously described methods (Ren et al., 2011). Briefly, adult mice were deeply anesthetized with intraperitonial (i.p.) injection of avertin (300 mg/kg) and transcardially perfused with ~5 ml of ice-cold oxygenated solution containing (in mM) 225 sucrose, 119 NaCl, 2.5 KCl, 1 NaH_2PO4, 4.9 $MgCl_2$, 0.1 $CaCl_2$, 26.2 $NaHCO_3$, 1.25 glucose, 3 kynurenic acid, and 1 Na-ascorbate (all chemicals were from Sigma, St Louis, MO, USA). Mice were then rapidly decapitated and whole brains were dissected into ice-cold oxygenated slicing solution containing (in mM) 110 choline chloride, 2.5 KCl, 0.5 $CaCl_2$, 7 $MgCl_2$, 1.3 NaH_2PO_4, 1.3 Na-ascorbate, 0.6 Na-pyruvate, 20 glucose, and 25 $NaHCO_3$ (saturated with 95% O_2 and 5% CO_2). Coronal brain sections (250 μm thick) containing DR were cut with a vibratome (VT1000s, Leica, Nussloch, Germany). Slices were incubated for at least 1 hr at 34°C in oxygenated artificial cerebrospinal fluid (aCSF) containing (in mM) 125 NaCl, 2.5 KCl, 2 $CaCl_2$, 1.3 $MgCl_2$, 1.3 NaH_2PO_4, 1.3 Na-ascorbate, 0.6 Napyruvate, 20 glucose, and 25 $NaHCO_3$. They were then transferred to a recording chamber on an upright Olympus fluorescent microscope equipped with differential interference contrast optics (DIC, COHU 4915–2000). During recording, slices were submerged and superfused (2 ml/min) with artificial cerebral spinal fluid (aCSF) at room temperature (22–24°C). Whole-cell recordings from DR serotonin neurons were obtained under visual control via DIC microscopy. Recording pipettes (4–7 MΩ) were backfilled with internal solution containing (in mM) 130 K-gluconate, 10 HEPES, 0.6 EGTA, 5 KCl, 3 Na_2ATP, 0.3 Na_3GTP, 4 $MgCl_2$, and 10 Na_2phosphocreatine (pH 7.2–7.4). Current-clamp recordings were carried out with a computer-controlled amplifier (MultiClamp 700B,

Molecular Devices); neurons were held at –58 mV. Traces were low-pass filtered at 2.6 kHz and digitized at 10 kHz (DigiData 1440, Molecular Devices). Data were acquired by Clampex 10.4 and analyzed using Clampfit 10.4 software (Molecular Devices). To quantify action potential firing frequency, at least five minutes of baseline activity were collected from each cell. 10 μM CNO was added into the aCSF perfusion circulation for 3 min, after which it was replaced by normal aCSF. Drug effects were measured by recording traces 5 min before and 10 min after drug perfusion. Action potential firing frequency was counted by the "event detection" function of Clampfit 10.4. Control recordings were performed as described above, but from $tdTomato^+$ neurons from Sert-Cre;Ai14 mice.

Local Field Potential Recordings and Current Source Density Analysis of Optogenetically-Evoked Responses—To examine how activation of serotonergic fibers modulates network activity in the orbital frontal cortex (OFC), we injected AAV_{DJ}-EF1-DIO-hChR2(H134R)-eYFP into the DR of 8 weeks male Sert-Cre mice. Five months later, acute slices containing the OFC were collected in accordance with the procedures described in (Makinson et al., 2017). Mice were anesthesized with pentobarbital (50 mg/kg) and perfused with ice-cold sucrose buffer containing (in mM): 234 sucrose, 2.5KCl, 1.25 NaH_2PO_4, 10 $MgSO_4$, 0.5 $CaCl_2$, 26 $NaHCO_3$, and 11 glucose, equilibrated with 95% O_2 and 5% CO_2, pH 7.4. Mice were decapitated, the brain dissected, and coronal slices (400 μm) were collected using a Leica VT1200S vibratome. Slices were transferred to oxygenated aCSF (containing in mM: 126 NaCl, 2.5 KCl, 1.25 NaH_2PO_4, 2 $MgCl_2$,2 $CaCl_2$, 26 $NaHCO_3$), bubbled continuously with 95% O_2 and 5% CO_2, and incubated at 32°C for 1 hour. Then, slices were incubated at room temperature for 1–5 hours before being placed in an interface recording chamber, in which they were continuously perfused with oxygenated aCSF (30–32°C) at a flow rate of 2–3ml/min.

A linear silicon multichannel probe (16 channels, 100 μm inter-electrode spacing, NeuroNexus Technologies) was placed in the OFC perpendicular to the laminar plane, such that the electrode array collected local field potentials (LFPs) from each cortical lamina. An optical fiber was situated immediately medial to the recording array directly above layer II/III to deliver 10 ms pulses of blue light (25 mW). Additionally, a bipolar tungsten electrode was placed in layer V to deliver electrical pulses (0.1 ms, 100 uA) to evoke synaptic responses and confirm the efficacy of drugs altering synaptic neurotransmission. Signals from all sixteen channels were digitized at 25 kHz using a 0–3000 Hz band-pass filter and amplified and stored using a RZ5D processor multichannel workstation (Tucker-Davis Technologies). A current source density (CSD) analysis was performed by calculating the second spatial derivative of the LFP (Nicholson and Freeman, 1975). This was used to estimate the magnitude, direction, and location of synaptic current recorded in the LFPs. When net positive current enters a cell, this creates an extracellular negativity reflected in a current "sink," and appears as a negative deflection in the CSD. Conversely, current "sources" indicate net negative current flowing into a cell and will create positive CSD responses.

To measure the baseline response, light pulses were delivered once a minute to activate ChR2 in DR fibers in the OFC, and LFPs were collected and averaged over at least 5 trials. To determine the contribution of different neurotransmitters to light-evoked LFPs, drugs

were bath applied for at least 30 minutes, and light responses were collected for another 5 trials. We utilized a cocktail of 5HT antagonists including GR 113808 (10 μM), Metergoline (10 μM), and Ondansetron (1 μM), and a separate cocktail of ionotropic glutamate receptor antagonists DNQX (25 μM) and CPP (1 μM). To avoid capturing a light artifact in our measurements, we extracted the average amplitude of the CSD over a 100 ms window measured 160 ms following the end of the light pulse. Control experiments in inactivated slices revealed that the light artifact coincided in time with the light pulse. LFP and CSD plots were generated using custom MATLAB scripts. Statistics were performed using SPSS 22 Statistics. For normal data, paired t tests were used to compare CSD amplitudes between baseline and drug conditions. For data without a normal distribution, a Wilcoxon Signed Rank test was used.

Drug Administration: Clozapine N-oxide (CNO; Cayman Chemical, Item No. 12059) was dissolved in 0.4% DMSO and 0.9% NaCl. We administered CNO by intraperitoneal injection with a lower dose (1 mg/kg) and gave it to all the groups of animals to diminish the possibility that the behavioral effects were caused by a CNO side effect rather than serotonin neuron activation. To achieve 1 mg/kg body weight when CNO was injected 40 min before the onset of behavioral tests (Teissier et al., 2015). According to the most recent report regarding the CNO and clozapine's influence on locomotion/anxiety related behavior test, there is no side effect when the dose of CNO is 1 mg/kg, but significant side-effect when the dose of CNO is 10 mg/kg. Only ~2% of CNO converts to clozapine after injection (Gomez et al., 2017), which means that the clozapine concentration in our experiments is likely to be ~0.02 mg/kg, far below 1 mg/kg clozapine that has been reported to elevate locomotor activity in the open field test.

Behavioral Assays—The behavioral assays described below are in the order of assay performance. Each assay was separated from the previous one by at least 5 days. All the mice that survived the surgery were included in the data analysis. One mouse died before all the assays were completed. Each groups comprised two to three cohorts.

Open field.: The open field apparatus consisted of a 50 cm x 50 cm clear Plexiglas arena. The intensity of the ambient light in the OFT is 199.3±0.5 LUX. Mice were acclimated to the experimental test room for at least 30 min prior to testing. To start a session, a mouse was placed in the center of the arena and allowed to freely explore for 10 minutes with video recording (Prut and Belzung, 2003). The total distance traveled (m), time spent in center (25 cm × 25 cm) (s) and center entries were automatically quantified by software (Biobserve).

Elevated plus maze.: The elevated plus maze apparatus consisted of two open and two closed arms extending out from a central platform. Each arm of the maze was 30 cm long and 5 cm wide. The maze surface was 85 cm above the floor. Each mouse was placed in the same position on the open arm of the maze at the beginning of the assay (facing the center) and allowed to explore the apparatus for 5 minutes (Walf and Frye, 2007). The number of open and closed arm entries as well as the total time spent in open and closed arms were automatically quantified by software (Biobserve).

Auditory fear conditioning.: The protocol was modified from previous studies (Do-Monte et al., 2015). Mice were habituated to the conditioning chamber and tones for 15 min per day for 3 days. On the fourth day, animals in gain-of-function experiments received a CNO injection 40 min before fear conditioning. The fear conditioning chamber consisted of a square cage (18 × 18 × 30 cm) with a floor wired to a shock generator and a scrambler, surrounded by an acoustic chamber (Coulbourn Instruments). We used two tones in a differential auditory fear conditioning protocol (CS+: 4 kHz, 30 sec, ~75 dB and CS–: 16 kHz, 30 sec, ~75 dB). The protocol consisted of 4 baseline tones (2 CS+, 2 CS–, interleaved), followed by interleaved presentations of 8x CS+ that co-terminated with a 1 s, 0.25 or 0.50 mA foot shock for gain- and loss-of-function experiments, respectively, and 4x CS– that were not paired with a foot shock. During a 1-day memory retrieval session, animals returned to the conditioning chamber and were presented with interleaved 8x CS+ and 4x CS–.

Forced-swim test.: Mice were placed for 6 min in a plastic cylinder (height: 25 cm; diameter: 18.5 cm) filled with water (15±1°C) to a depth of 14 cm. The water depth was adjusted so that the animals were forced to swim or float without their hind limbs touching the bottom. The sessions were videotaped and independently analyzed by two researchers blind to genotype. Duration of immobility (the time during which the subject made only the minimal movements necessary to keep their heads above water) was scored by averaging the results from the two researchers. A two-day forced-swim test was applied. For gain-of-function experiments, mice only received one CNO injection 40 min before the 2nd day test.

QUANTIFICATION AND STATISTICAL ANALYSIS

Quantification of anatomical, fiber photometry, electrophysiological recording and behavior tests data is described in corresponding section of text and methods details. All statistical tests and data analyses were performed using MATLAB and GraphPad Prism. Data were expressed as means ± SEMs in figures and text. Group differences were detected using either one-way analysis of variance (ANOVA), or with two-way ANOVA, both followed by Holm-Sidak test. According to histogram of dependent variable, the distributions of data meet normality assumption. Bartlett's test shows no significant difference among variance of groups. Multiple comparisons were corrected when appropriate by adjusting pvalues using the Holm-Sidak method. Significance was defined as $p<0.05$. Sample sizes were chosen based on those used in previous papers. Full details of each statistical test used (tests, statistics, significance levels, sample sizes, animal numbers, SEMs, and degrees of freedom) are described in each figure legend, except for Figure 4 and S4, which are listed in Table S3.

Supplementary Material

Refer to Web version on PubMed Central for supplementary material.

Acknowledgement:

We thank E. Adams and M. Tessier-Lavigne for advice on iDISCO+, T. Davidson and K. Deisseroth for advice on fiber photometry, E. Steinberg and R. Malenka for advice on behavior, Q. Wu for *Tph2*$^{flox/flox}$ mice, A. Karpova for the AAV_{retro} vector, Stanford, Salk, and UNC Viral Core for viruses, Allen Institute for the reference atlas and T. Gilbert for the advice on its use, M. Chen for code files for data analysis, K. Beier and G. Nachtrab for sharing

AAVs, S. Bell for advice on 2D registration, and R. Malenka, A. Mizrahi, A. Shuster, L. DeNardo, J. Lui, M. Wagner, and W. Allen for critiques on the manuscript. This work was supported by BRAIN initiative grants (R01 NS104698, NeuroNex). L.L. is an HHMI investigator.

Abbreviations for anatomical regions

AI	anterior insular cortex
BLA	basolateral amygdala
BNST	bed nucleus of the stria terminalis
CeA	central amygdala
CoA	cortical amygdala
DB	nucleus of the diagonal band
DCN	deep cerebellum nuclei
dLGN	dorsal lateral geniculate nucleus
ENT	entorhinal cortex
LHb	lateral habenula
LHy	lateral hypothalamus
NST	nucleus of solitary tract
OB	olfactory bulb
OFC	orbitofrontal cortex
PIR	piriform cortex
PSTh	parasubthalamic nucleus
PVH	paraventricular hypothalamus
PVHd	paraventricular hypothalamus, descending division
SI	substantia innominate
SNc	substantia nigra compacta
SNr	substantia nigra pars reticulate
Sth	subthalamic nucleus
VLPO	ventrolateral preoptic nucleus

References

Abrams JK, Johnson PL, Hollis JH, and Lowry CA (2004). Anatomic and functional topography of the dorsal raphe nucleus. Ann N Y Acad Sci 1018, 46–57. [PubMed: 15240351]

Albert PR, Vahid-Ansari F, and Luckhart C (2014). Serotonin-prefrontal cortical circuitry in anxiety and depression phenotypes: pivotal role of pre- and post-synaptic 5-HT1A receptor expression. Front Behav Neurosci 8, 199. [PubMed: 24936175]

Allen Brain Atlas (2017). Projection :: Allen Brain Atlas: Mouse Connectivity.

Allen Institute for Brain Science (2015). Allen Brain Atlas API.

Allen WE, DeNardo LA, Chen MZ, Liu CD, Loh KM, Fenno LE, Ramakrishnan C, Deisseroth K, and Luo L (2017). Thirst-associated preoptic neurons encode an aversive motivational drive. Science 357, 1149–1155. [PubMed: 28912243]

Armbruster BN, Li X, Pausch MH, Herlitze S, and Roth BL (2007). Evolving the lock to fit the key to create a family of G protein-coupled receptors potently activated by an inert ligand. Proc Natl Acad Sci U S A 104, 5163–5168. [PubMed: 17360345]

Azmitia EC, and Segal M (1978). An autoradiographic analysis of the differential ascending projections of the dorsal and median raphe nuclei in the rat. J Comp Neurol 179, 641–667. [PubMed: 565370]

Barnes NM, and Sharp T (1999). A review of central 5-HT receptors and their function. Neuropharmacology 38, 1083–1152. [PubMed: 10462127]

Beier KT, Kim CK, Hoerbelt P, Hung LW, Heifets BD, DeLoach KE, Mosca TJ, Neuner S, Deisseroth K, Luo L, et al. (2017). Rabies screen reveals GPe control of cocaine-triggered plasticity. Nature 549, 345–350. [PubMed: 28902833]

Beier KT, Steinberg EE, DeLoach KE, Xie S, Miyamichi K, Schwarz L, Gao XJ, Kremer EJ, Malenka RC, and Luo L (2015). Circuit Architecture of VTA Dopamine Neurons Revealed by Systematic Input-Output Mapping. Cell 162, 622–634. [PubMed: 26232228]

Belmaker RH, and Agam G (2008). Major depressive disorder. N Engl J Med 358, 55–68. [PubMed: 18172175]

Calhoon GG, and Tye KM (2015). Resolving the neural circuits of anxiety. Nat Neurosci 18, 1394–1404. [PubMed: 26404714]

Calizo LH, Akanwa A, Ma X, Pan YZ, Lemos JC, Craige C, Heemstra LA, and Beck SG (2011). Raphe serotonin neurons are not homogenous: electrophysiological, morphological and neurochemical evidence. Neuropharmacology 61, 524–543. [PubMed: 21530552]

Cohen JY, Amoroso MW, and Uchida N (2015). Serotonergic neurons signal reward and punishment on multiple timescales. Elife 4.

Commons KG (2015). Two major network domains in the dorsal raphe nucleus. J Comp Neurol 523, 1488–1504. [PubMed: 25652113]

Correia PA, Lottem E, Banerjee D, Machado AS, Carey MR, and Mainen ZF (2017). Transient inhibition and long-term facilitation of locomotion by phasic optogenetic activation of serotonin neurons. Elife 6.

Dayan P, and Huys Q (2015). Serotonin's many meanings elude simple theories. Elife 4.

Do-Monte FH, Quinones-Laracuente K, and Quirk GJ (2015). A temporal shift in the circuits mediating retrieval of fear memory. Nature 519, 460–463. [PubMed: 25600268]

Fernandez SP, Cauli B, Cabezas C, Muzerelle A, Poncer JC, and Gaspar P (2016). Multiscale single-cell analysis reveals unique phenotypes of raphe 5-HT neurons projecting to the forebrain. Brain Struct Funct 221, 4007–4025. [PubMed: 26608830]

Fonseca MS, Murakami M, and Mainen ZF (2015). Activation of Dorsal Raphe Serotonergic Neurons Promotes Waiting but Is Not Reinforcing. Curr Biol 25, 306–315. [PubMed: 25601545]

Franklin KBJ, and Paxinos G (2013). Paxinos and Franklin's The mouse brain in stereotaxic coordinates, Fourth edition edn (Amsterdam: Academic Press, an imprint of Elsevier).

Gagnon D, and Parent M (2014). Distribution of VGLUT3 in highly collateralized axons from the rat dorsal raphe nucleus as revealed by single-neuron reconstructions. PLoS One 9, e87709. [PubMed: 24504335]

Gomez JL, Bonaventura J, Lesniak W, Mathews WB, Sysa-Shah P, Rodriguez LA, Ellis RJ, Richie CT, Harvey BK, Dannals RF, et al. (2017). Chemogenetics revealed: DREADD occupancy and activation via converted clozapine. Science 357, 503–507. [PubMed: 28774929]

Gong S, Doughty M, Harbaugh CR, Cummins A, Hatten ME, Heintz N, and Gerfen CR (2007). Targeting Cre recombinase to specific neuron populations with bacterial artificial chromosome constructs. J Neurosci 27, 9817–9823. [PubMed: 17855595]

Gras C, Herzog E, Bellenchi GC, Bernard V, Ravassard P, Pohl M, Gasnier B, Giros B, and El Mestikawy S (2002). A third vesicular glutamate transporter expressed by cholinergic and serotoninergic neurons. J Neurosci 22, 5442–5451. [PubMed: 12097496]

Grimes WN, Seal RP, Oesch N, Edwards RH, and Diamond JS (2011). Genetic targeting and physiological features of VGLUT3+ amacrine cells. Vis Neurosci 28, 381–392. [PubMed: 21864449]

Gunaydin LA, Grosenick L, Finkelstein JC, Kauvar IV, Fenno LE, Adhikari A, Lammel S, Mirzabekov JJ, Airan RD, Zalocusky KA, et al. (2014). Natural neural projection dynamics underlying social behavior. Cell 157, 1535–1551. [PubMed: 24949967]

Ishimura K, Takeuchi Y, Fujiwara K, Tominaga M, Yoshioka H, and Sawada T (1988). Quantitative analysis of the distribution of serotonin-immunoreactive cell bodies in the mouse brain. Neurosci Lett 91, 265–270. [PubMed: 3185964]

Klein S, Staring M, Murphy K, Viergever MA, and Pluim JP (2010). elastix: a toolbox for intensity-based medical image registration. IEEE Trans Med Imaging 29, 196–205. [PubMed: 19923044]

Lein ES, Hawrylycz MJ, Ao N, Ayres M, Bensinger A, Bernard A, Boe AF, Boguski MS, Brockway KS, Byrnes EJ, et al. (2007). Genome-wide atlas of gene expression in the adult mouse brain. Nature 445, 168–176. [PubMed: 17151600]

Li Y, Zhong W, Wang D, Feng Q, Liu Z, Zhou J, Jia C, Hu F, Zeng J, Guo Q, et al. (2016). Serotonin neurons in the dorsal raphe nucleus encode reward signals. Nat Commun 7, 10503. [PubMed: 26818705]

Liu ZX, Zhou JF, Li Y, Hu F, Lu Y, Ma M, Feng QR, Zhang JE, Wang DQ, Zeng JW, et al. (2014). Dorsal Raphe Neurons Signal Reward through 5-HT and Glutamate. Neuron 81, 1360–1374. [PubMed: 24656254]

Lowry CA, Johnson PL, Hay-Schmidt A, Mikkelsen J, and Shekhar A (2005). Modulation of anxiety circuits by serotonergic systems. Stress 8, 233–246. [PubMed: 16423712]

Madisen L, Zwingman TA, Sunkin SM, Oh SW, Zariwala HA, Gu H, Ng LL, Palmiter RD, Hawrylycz MJ, Jones AR, et al. (2010). A robust and high-throughput Cre reporting and characterization system for the whole mouse brain. Nat Neurosci 13, 133–140. [PubMed: 20023653]

Marcinkiewcz CA, Mazzone CM, D'Agostino G, Halladay LR, Hardaway JA, DiBerto JF, Navarro M, Burnham N, Cristiano C, Dorrier CE, et al. (2016). Serotonin engages an anxiety and fear-promoting circuit in the extended amygdala. Nature 537, 97–101. [PubMed: 27556938]

Makinson CD, Tanaka BS, Sorokin JM, Wong JC, Christian CA, Goldin AL, Escayg A, and Huguenard JR (2017). Regulation of Thalamic and Cortical Network Synchrony by Scn8a. Neuron 93, 1165–1179 e1166. [PubMed: 28238546]

Meltzer HY (1994). An overview of the mechanism of action of clozapine. J Clin Psychiatry 55 Suppl B, 47–52. [PubMed: 7961573]

Miyazaki KW, Miyazaki K, and Doya K (2012). Activation of Dorsal Raphe Serotonin Neurons Is Necessary for Waiting for Delayed Rewards. J Neurosci 32, 10451–10457. [PubMed: 22855794]

Muller CP, and Jacobs BL (2010). Handbook of the Behavioral Neurobiology of Serotonin (Elsevier).

Muzerelle A, Scotto-Lomassese S, Bernard JF, Soiza-Reilly M, and Gaspar P (2016). Conditional anterograde tracing reveals distinct targeting of individual serotonin cell groups (B5–B9) to the forebrain and brainstem. Brain Struct Funct 221, 535–561. [PubMed: 25403254]

Neve RL, Neve KA, Nestler EJ, and Carlezon WA, Jr. (2005). Use of herpes virus amplicon vectors to study brain disorders. Biotechniques 39, 381–391. [PubMed: 16206910]

Nicholson C, and Freeman JA (1975). Theory of current source-density analysis and determination of conductivity tensor for anuran cerebellum. J Neurophysiol 38, 356–368. [PubMed: 805215]

Niederkofler V, Asher TE, Okaty BW, Rood BD, Narayan A, Hwa LS, Beck SG, Miczek KA, and Dymecki SM (2016). Identification of Serotonergic Neuronal Modules that Affect Aggressive Behavior. Cell Reports 17, 1934–1949. [PubMed: 27851959]

Ogawa SK, Cohen JY, Hwang D, Uchida N, and Watabe-Uchida M (2014). Organization of monosynaptic inputs to the serotonin and dopamine neuromodulatory systems. Cell Rep 8, 1105–1118. [PubMed: 25108805]

Oh SW, Harris JA, Ng L, Winslow B, Cain N, Mihalas S, Wang Q, Lau C, Kuan L, Henry AM, et al. (2014). A mesoscale connectome of the mouse brain. Nature 508, 207–214. [PubMed: 24695228]

Okaty BW, Freret ME, Rood BD, Brust RD, Hennessy ML, deBairos D, Kim JC, Cook MN, and Dymecki SM (2015). Multi-Scale Molecular Deconstruction of the Serotonin Neuron System. Neuron 88, 774–791. [PubMed: 26549332]

Petit-Demouliere B, Chenu F, and Bourin M (2005). Forced swimming test in mice: a review of antidepressant activity. Psychopharmacology (Berl) 177, 245–255. [PubMed: 15609067]

Pollak Dorocic I, Furth D, Xuan Y, Johansson Y, Pozzi L, Silberberg G, Carlen M, and Meletis K (2014). A whole-brain atlas of inputs to serotonergic neurons of the dorsal and median raphe nuclei. Neuron 83, 663–678. [PubMed: 25102561]

Prouty EW, Chandler DJ, and Waterhouse BD (2017). Neurochemical differences between target-specific populations of rat dorsal raphe projection neurons. Brain Res 1675, 28–40. [PubMed: 28867482]

Prut L, and Belzung C (2003). The open field as a paradigm to measure the effects of drugs on anxiety-like behaviors: a review. Eur J Pharmacol 463, 3–33. [PubMed: 12600700]

Ravindran LN, and Stein MB (2010). The pharmacologic treatment of anxiety disorders: a review of progress. J Clin Psychiatry 71, 839–854. [PubMed: 20667290]

Ren J, Qin C, Hu F, Tan J, Qiu L, Zhao S, Feng G, and Luo M (2011). Habenula “cholinergic” neurons co-release glutamate and acetylcholine and activate postsynaptic neurons via distinct transmission modes. Neuron 69, 445–452. [PubMed: 21315256]

Renier N, Adams EL, Kirst C, Wu Z, Azevedo R, Kohl J, Autry AE, Kadiri L, Umadevi Venkataraju K, Zhou Y, et al. (2016). Mapping of Brain Activity by Automated Volume Analysis of Immediate Early Genes. Cell 165, 1789–1802. [PubMed: 27238021]

Schwarz LA, Miyamichi K, Gao XJ, Beier KT, Weissbourd B, DeLoach KE, Ren J, Ibanes S, Malenka RC, Kremer EJ, et al. (2015). Viral-genetic tracing of the input-output organization of a central noradrenaline circuit. Nature 524, 88–92. [PubMed: 26131933]

Sengupta A, Bocchio M, Bannerman DM, Sharp T, and Capogna M (2017). Control of Amygdala Circuits by 5-HT Neurons via 5-HT and Glutamate Cotransmission. J Neurosci 37, 1785–1796. [PubMed: 28087766]

Shamonin DP, Bron EE, Lelieveldt BP, Smits M, Klein S, Staring M, and Alzheimer’s Disease Neuroimaging I (2013). Fast parallel image registration on CPU and GPU for diagnostic classification of Alzheimer’s disease. Front Neuroinform 7, 50. [PubMed: 24474917]

Steinbusch HW (1981). Distribution of serotonin-immunoreactivity in the central nervous system of the rat-cell bodies and terminals. Neuroscience 6, 557–618. [PubMed: 7017455]

Teissier A, Chemiakine A, Inbar B, Bagchi S, Ray RS, Palmiter RD, Dymecki SM, Moore H, and Ansorge MS (2015). Activity of Raphe Serotonergic Neurons Controls Emotional Behaviors. Cell Rep 13, 1965–1976. [PubMed: 26655908]

Tervo DG, Hwang BY, Viswanathan S, Gaj T, Lavzin M, Ritola KD, Lindo S, Michael S, Kuleshova E, Ojala D, et al. (2016). A Designer AAV Variant Permits Efficient Retrograde Access to Projection Neurons. Neuron 92, 372–382. [PubMed: 27720486]

Urban DJ, Zhu H, Marcinkiewcz CA, Michaelides M, Oshibuchi H, Rhea D, Aryal DK, Farrell MS, Lowery-Gionta E, Olsen RHJ, et al. (2016). Elucidation of The Behavioral Program and Neuronal Network Encoded by Dorsal Raphe Serotonergic Neurons. Neuropsychopharmacol 41, 1404–1415.

Vertes RP (1991). A PHA-L analysis of ascending projections of the dorsal raphe nucleus in the rat. J Comp Neurol 313, 643–668. [PubMed: 1783685]

Walf AA, and Frye CA (2007). The use of the elevated plus maze as an assay of anxiety-related behavior in rodents. Nat Protoc 2, 322–328. [PubMed: 17406592]

Warden MR, Selimbeyoglu A, Mirzabekov JJ, Lo M, Thompson KR, Kim SY, Adhikari A, Tye KM, Frank LM, and Deisseroth K (2012). A prefrontal cortex-brainstem neuronal projection that controls response to behavioural challenge. Nature 492, 428–432. [PubMed: 23160494]

Waselus M, Valentino RJ, and Van Bockstaele EJ (2011). Collateralized dorsal raphe nucleus projections: a mechanism for the integration of diverse functions during stress. J Chem Neuroanat 41, 266–280. [PubMed: 21658442]

Weissbourd B, Ren J, DeLoach KE, Guenthner CJ, Miyamichi K, and Luo L (2014). Presynaptic partners of dorsal raphe serotonergic and GABAergic neurons. Neuron 83, 645–662. [PubMed: 25102560]

Whitney MS, Shemery AM, Yaw AM, Donovan LJ, Glass JD, and Deneris ES (2016). Adult Brain Serotonin Deficiency Causes Hyperactivity, Circadian Disruption, and Elimination of Siestas. J Neurosci 36, 9828–9842. [PubMed: 27656022]

Wickersham IR, Finke S, Conzelmann KK, and Callaway EM (2007). Retrograde neuronal tracing with a deletion-mutant rabies virus. Nat Methods 4, 47–49. [PubMed: 17179932]

World Health Organization (2017). Depression.

Wu Q, Clark MS, and Palmiter RD (2012). Deciphering a neuronal circuit that mediates appetite. Nature 483, 594–597. [PubMed: 22419158]

Xiong J, Ren J, Luo L, Horowitz AM (2018). Mapping Mouse Brain Slice Sequence to a Reference Brain Without 3D Reconstruction. bioRxiv doi:10.1101/357475

- Dorsal raphe (DR) serotonin neurons are organized into parallel sub-systems
- OFC- and CeA-projecting DR serotonin neurons have complementary collateralizations
- OFC- and CeA-projecting DR serotonin neurons respond oppositely to aversive stimuli
- OFC- and CeA-projecting DR serotonin neurons have distinct behavioral functions

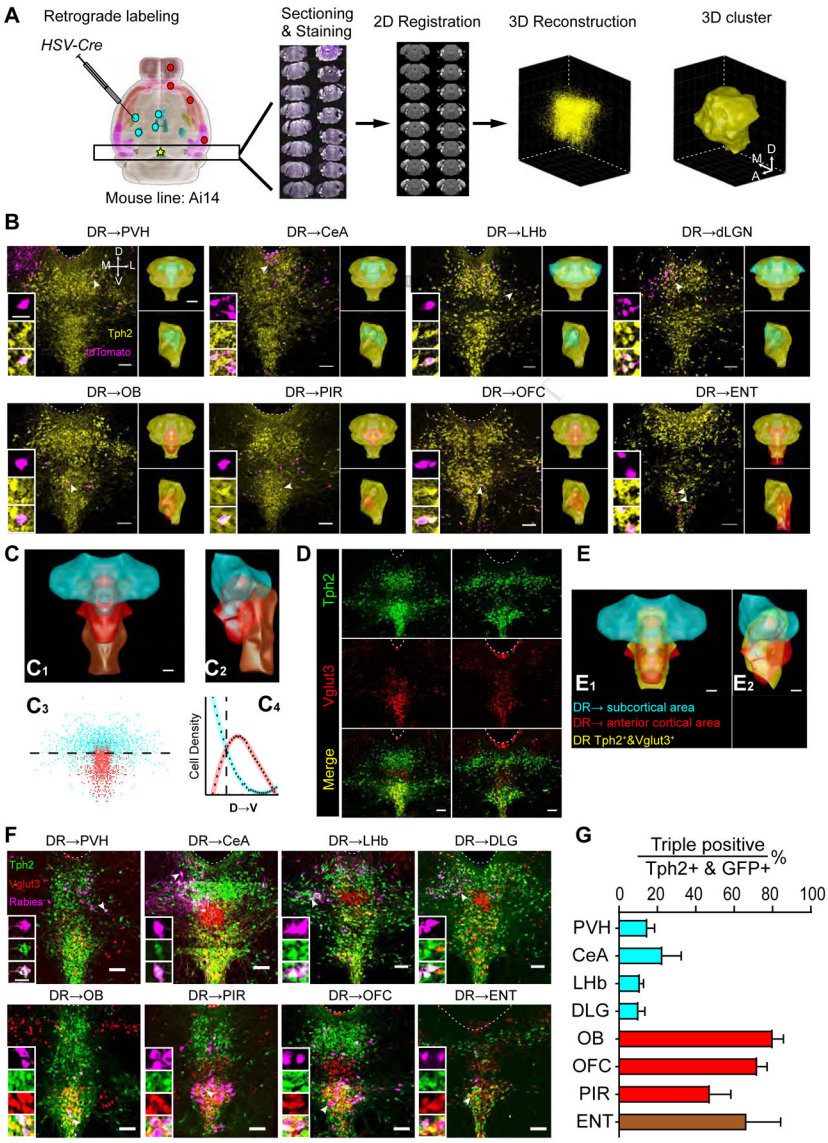

Figure 1. Spatial Organization of DR Serotonin Neurons according to Axonal Projections and Vglut3 Co-expression

(A) Schematic of retrograde labeling and 3D reconstruction of spatial locations of DR serotonin neurons. Cyan and red dots represent injection sites of *HSV-Cre* in *Ai14* mice. Anti-Tph2 staining was performed on consecutive coronal sections containing DR (star). The positions of $Tph2^+$/$tdTomato^+$ cells were recorded in confocal images. Each section was registered to the Allen reference brain and reconstructed in 3D. DBSCAN was applied for spatial clustering to generate a 3D surface based on the location of $Tph2^+$ neurons (STAR Methods).

(B) Representative coronal confocal sections of the DR. Magenta, retrogradely labeled cells from eight projecting sites; yellow, anti-Tph2 staining. Dashed line, aqueduct border. Scale, 100 μm. Left insets, high-magnification images of neurons marked by arrows in individual channels. Scale, 25 μm. Right insets (top, coronal view; bottom, sagittal view): yellow, cyan, and red structures represent 3D surface of the clusters of, respectively, all DR $Tph2^+$

neurons; those that project to PVH/CeA/LHb/dLGN; or those that project to OB/PIR/OFC/ENT. Scale, 500 μm.

(C) Merged surface view of the DR^{Tph2}→SC (subcortical) cluster (cyan), →AC (anterior cortex) cluster (red), and →ENT cluster (brown) in coronal (C_1) and sagittal (C_2) view. Scale, 200 μm. C_3, coronal projection showing the location of individual cells from the DR^{Tph2}→SC and →AC groups. C_4, densities of DR^{Tph2}→SC and →AC neurons along D–V axis. The two clusters exhibit the same line density at a horizontal plane 3742 μm ventral to the brain surface (dashed line). 74% of DR^{Tph2}→SC neurons were dorsal to this plane, whereas 80% of DR^{Tph2}→AC neurons were ventral to this plane.

(D) Representative coronal confocal sections of DR showing anti-Tph2 staining in *Vglut3-Cre/Ai14* mice (green), which express tdTomato in $Vglut3^+$ cells (red).

(E) Coronal (E_1) and sagittal (E_2) view integrating projection-defined clusters and the cluster of $Tph2^+$&$Vlgut3^+$ neurons (yellow, 1730±219.8 neurons; n=3). Scale, 200 μm.

(F) Representative coronal confocal sections of the DR showing retrograde labeling neurons from eight brain regions (magenta, pseudo-colored from rabies-derived GFP), anti-Tph2 staining (green), and tdTomato from Vglut3-Cre^+ neurons (red). Scale, 100 μm. Insets: magnified images showing the neurons indicated with arrows in individual channels. Scale, 25 μm.

(G) The proportion of GFP, Tph2, and Vglut3 triple positive neurons in $GFP^+/Tph2^+$ neurons for 8 projection brain regions.

In this and all subsequent figures, abbreviations for anatomical regions can be found in Methods. Axis labels: A, anterior; P, posterior, D, dorsal; V, ventral; M, medial; L, lateral. Error bars, SEM.

See Figure S1 for related data, and Table S4 for cell numbers labeled by retrograde tracers.

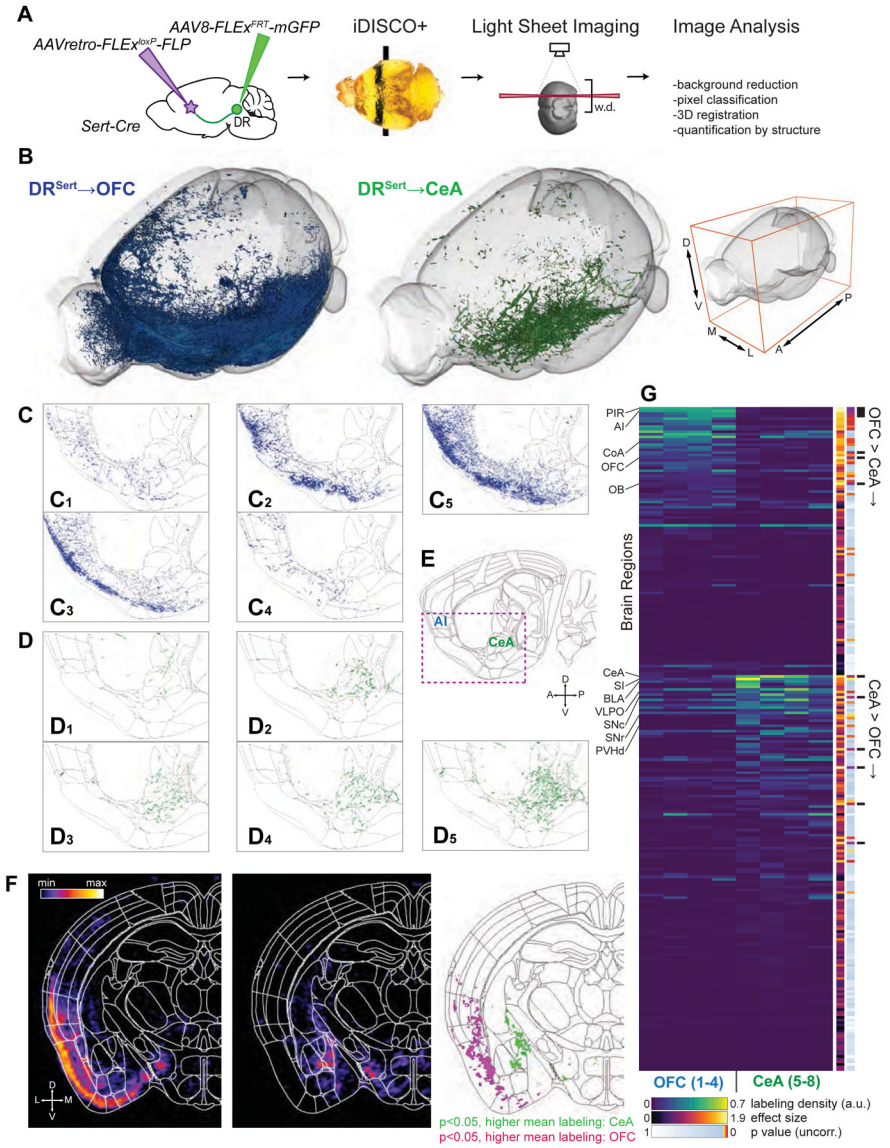

Figure 2. Distinct Collateralization Patterns of DR^{Sert}→OFC and DR^{Sert}→CeA Neurons

(A) Schematic of viral-genetic tracing and whole-brain 3D imaging. w.d., working distance of the light-sheet microscope objective.

(B) Overview of axonal projections from one representative brain each from the DR^{Sert}→OFC (blue) and DR^{Sert}→CeA (green) groups. Whole-mount imaging included the entire left hemisphere and the medial-most ~650 μm of the right hemisphere. Axes as indicated on right. See Movie S2 for a 3D rendering.

(C, D) Sagittal view of single 5-μm optical sections from eight individual brains registered to the Allen Institute common coordinate framework. Axons from DR^{Sert}→OFC (C_1–C_4; merged in C_5) and DR^{Sert}→CeA (D_1–D_4; merged in D_5) neurons are shown in green and blue, respectively.

(E) Sagittal brain atlas image (10 μm) from the Allen Institute that encompasses CeA and anterior insular cortex (AI). The red box indicates the displayed region of (C) and (D).</p/

>(F) Coronal density maps of $DR^{Sert}\rightarrow$CeA (left) and $DR^{Sert}\rightarrow$OFC (middle) projections generated by voxel-wise dilation of axons. Right, a p-value map highlighting individual voxels with $p<0.05$ between groups. See Movie S3 for the fly-through of coronal maps of the brain rostral to DR.

(G) Heat map of relative labeling density (normalized to region volume and gross label content per brain) across 255 regions defined by the Allen Atlas. Additional columns show statistics for effect size, uncorrected p-values from two-tailed t-tests, and findings that pass false discovery rate at 10% (black bars). See Table S1 for the list of brain regions in the same sequence.

See Figure S2 and Table S1 for related data.

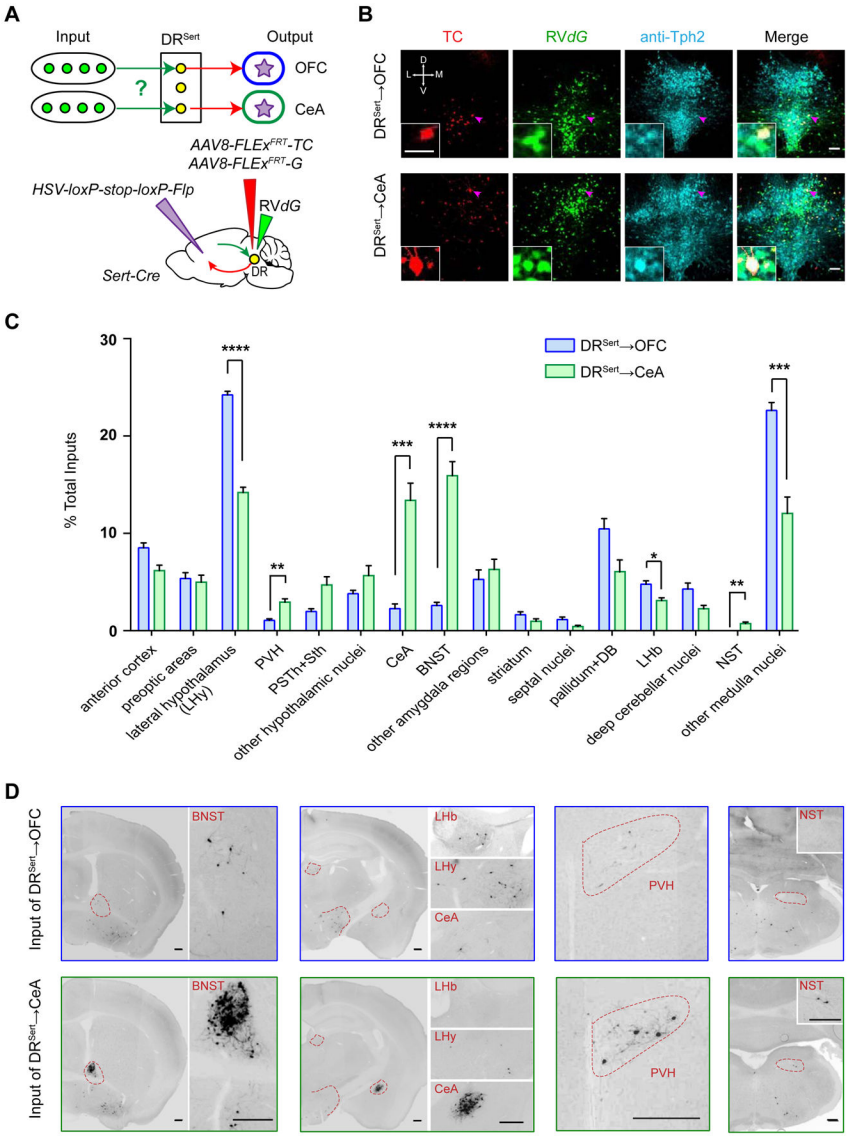

Figure 3. Biased Input Distributions for DR^{Sert}→OFC and DR^{Sert}→CeA Neurons

(A) Schematic of cTRIO experiments.

(B) Confocal images of coronal sections containing the DR, showing OFC- and CeA-projecting serotoninergic starter cells (starter cell numbers for DR^{Sert}→OFC: 73±8.3, n=9 mice; for DR^{Sert}→CeA: 96±13.4, n=8 mice). Red, TVA-mCherry (TC) expression; green, GFP expression; cyan, anti-Tph2 staining. Scale, 100 μm. Insets: high magnification images of neurons indicated by arrows. Scale, 50 μm.

(C) Quantification of whole-brain inputs to DR^{Sert}→OFC and DR^{Sert}→CeA neurons (n=9, 8). Y-axis presents percentage of total inputs counted for each brain. Error bars, SEM. *p<0.05, **p<0.01, ***p<0.001 and ****p<0.0001 (multiple t-tests with Holm-Sidak correction).

(D) Representative GFP labeled ipsilateral input cells to DR^{Sert}→OFC and DR^{Sert}→CeA neurons. Scale, 250 μm.

See Figures S3 and Table S2 for related data.

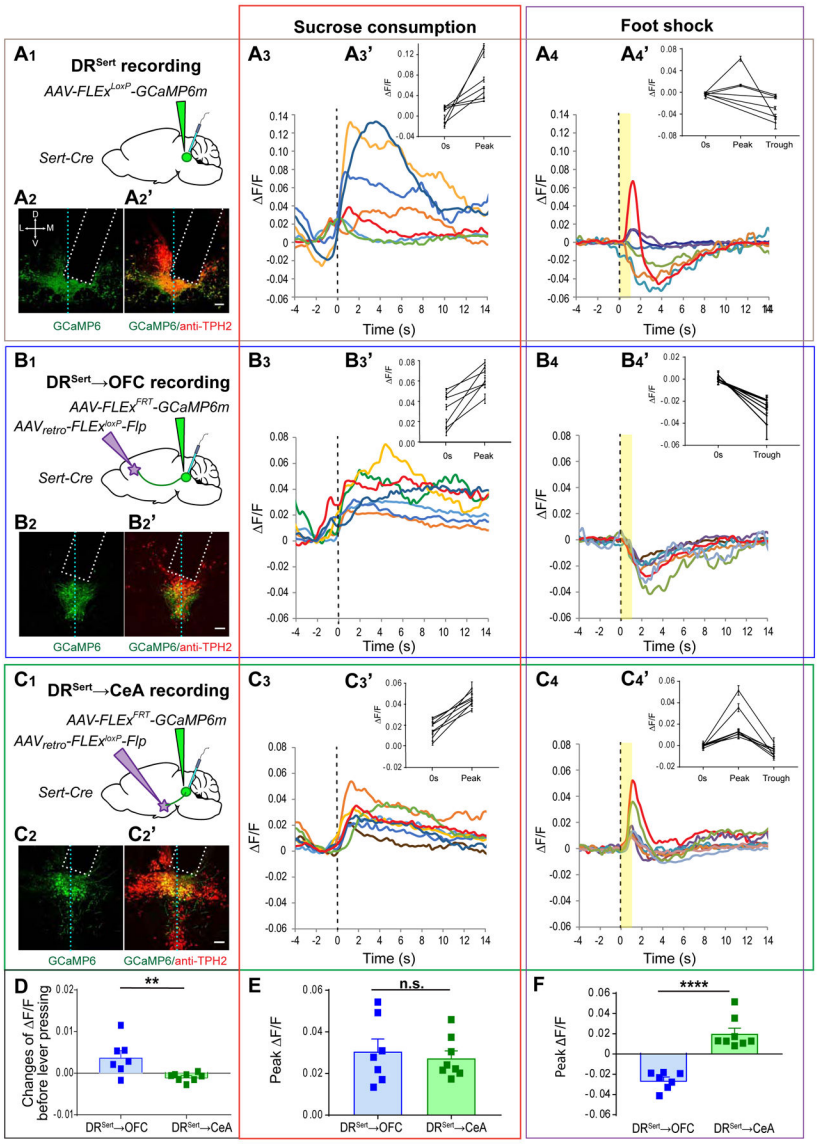

Figure 4. DR^{Sert}→OFC and DR^{Sert}→CeA Neurons Are Both Activated by Reward but Show Opposite Responses to Punishment.

Fiber photometry recordings were performed on DR^{Sert} (A), DR^{Sert}→OFC (B) and DR^{Sert}→CeA (C) neurons.

(A_1–C_1) Schematic of viral injection and optical fiber (cyan) implantation.

(A_2–C_2) Confocal images of coronal sections showing fiber optic placement (dotted rectangle) and the expression of GCaMP6m (green) with Tph2 staining (red, A_2'–C_2') in the DR. Vertical dashed lines represent the midline. Scale, 100 μm. Estimate of GCaMP6m$^+$ serotonin neurons under optical fiber: DR^{Sert} group, 204±39.0, n=7 mice; DR^{Sert}→OFC group, 112±28.0, n=7 mice; DR^{Sert}→CeA group, 115±22.1, n=8 mice.

(A_3–C_3) Mean responses of individual mice to sucrose consumption after lever press. Time 0 is aligned to lick initiation (vertical dashed line). Red traces correspond to the mice shown in (A_2–C_2) and Figure S4. (A_3'–C_3') Group data from all trials of individual mice showing

quantification of the peak *ΔF/F* during sucrose water licking comparing to the *ΔF/F* at time 0 (paired t test; $p<0.001$ for all comparisons; $n\geq20$ trials).

(A_4–C_4) Mean responses of individual mice from the three groups to electrical shock. Time 0 is aligned to onset of 1-sec electric shock delivery. (A_4'–C_4') Group data from all the trials of individual mice showing quantification of the peak *ΔF/F* (positive extreme) and trough *ΔF/F* (negative extreme) recorded after electric shock delivery comparing to the *ΔF/F* at time (B_4', two-tailed paired t test, $p<0.01$ for all comparisons in inhibition. C_4', one-way ANOVA followed by multiple t-test, $p<0.05$ for all comparisons in activation. n=12 trials).

(D) Quantification of integrated *ΔF/F* signals between 0.13s to 0.65s before lever press (after subtracting integrated signals between 0.65s and 0.117s before lever press) comparing $DR^{Sert}\rightarrow$OFC and $DR^{Sert}\rightarrow$CeA neurons.

(E) Quantification of the peak *ΔF/F* recorded during sucrose water licking from $DR^{Sert}\rightarrow$OFC and $DR^{Sert}\rightarrow$CeA neurons.

(F) Quantification of the peak *ΔF/F* (negative or positive extreme) recorded after electric shock delivery from $DR^{Sert}\rightarrow$OFC and $DR^{Sert}\rightarrow$CeA neurons.

Error bars, SEM; n.s., not significant; *p<0.05; **p<0.01; ***p<0.001; ***p<0.001; ****p<0.0001. (For D–F, unpaired t-test; n=7, 8 mice for $DR^{Sert}\rightarrow$OFC and $DR^{Sert}\rightarrow$CeA groups, respectively).

See Figures S4 and Table S3 for related data.

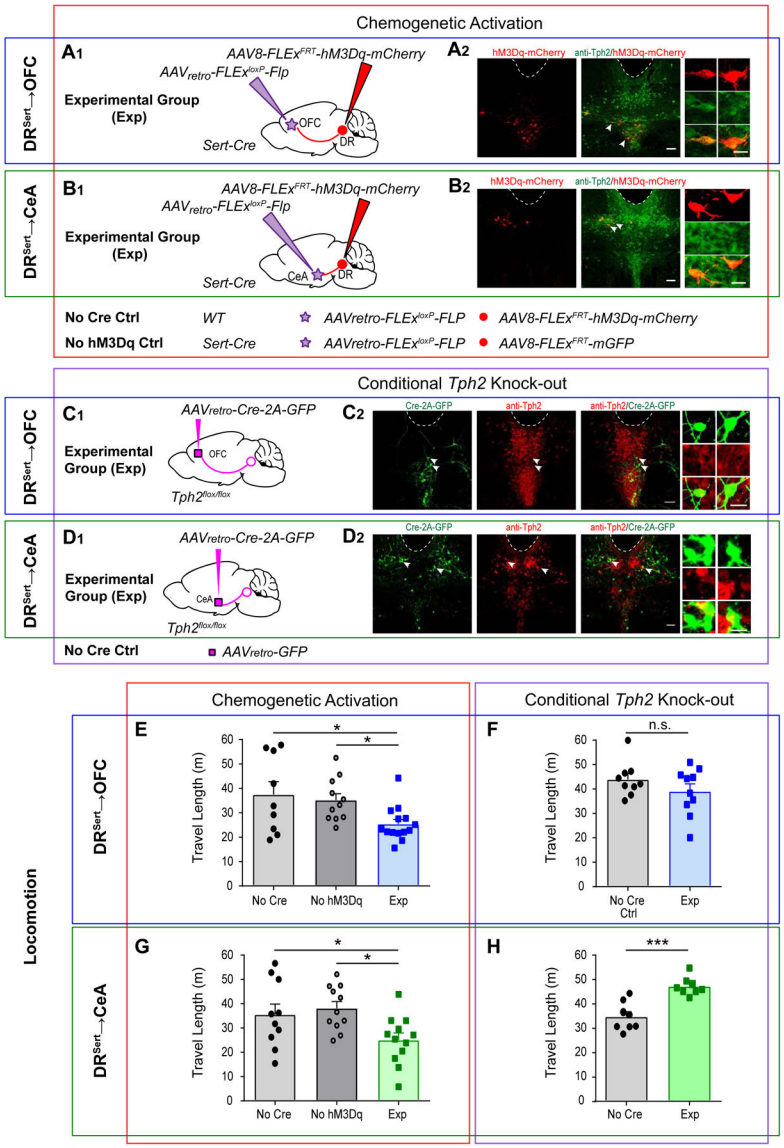

Figure 5. Chemogenetic Activation and Conditional *Tph2* Knockout Reveal that Both DR^{Sert}→OFC and DR^{Sert}→CeA Neurons Suppress Locomotion.

(A, B) Chemogenetic activation of DR^{Sert}→OFC (A) and DR^{Sert}→CeA (B) neurons. (A_1, B_1) Schematic for experimental (Exp) groups. Conditions for the two controls (Ctrl) are listed below. (A_2, B_2) Confocal images of coronal sections showing the expression of hM3Dq-2A-mCherry (red), and co-labeling with Tph2 staining (green) in the DR. Dotted lines are aqueduct borders. Scale, 100 μm. Right, high magnification images of neurons indicated by arrows. Scale, 50 μm. See Table S4 for cell counts.

(C, D) DR^{Sert}→OFC (C) and DR^{Sert}→CeA (D) neurons were Tph2 depleted by bilaterally injecting *AAV$_{retro}$-Cre* into OFC (C_1) or CeA (D_1) of the *Tph2$^{flox/flox}$* mice. (C_2, D_2) Confocal images of coronal sections showing the expression of Cre-2A-GFP (green), almost all of which were negative from Tph2 staining (red) in the DR. (Cells counts: Exp DR^{Sert}→OFC group, 272±67.9, 98.6%±0.43% were Tph2^{-}; Exp DR^{Sert}→CeA group, 331±76.6, 98.7%±0.33% were Tph2^{-}. Ctrl DR^{Sert}→OFC group, 160±8.5, 16.7%±0.18%

were Tph2^{-}; Ctrl DR^{Sert}→CeA group, 177±42.2, 39.2%±0.16% were Tph2^{-}; n=3 mice for all groups). Scale, 100 μm. Right, high magnification images showing neurons indicated by arrows. Scale, 25 μm.

(E) Chemogenetic activation of DR^{Sert}ÍOFC neurons decreases distance traveled (one-way ANOVA followed by multiple t-tests; F(2, 31) = 4.42, t=2.672, 2.29. n= 9, 11, 14). *p<0.05.

(F) Conditionally knocking out *Tph2* from DR^{Sert}ÍOFC neurons does not have a significant effect on distance traveled (two-tail unpaired t-test, t=1.24, df=17; n=9, 10).

(G) Activation of DR^{Sert}→CeA neurons decreases distance traveled (one-way ANOVA followed by multiple t-test; F(2, 30) = 4.516; t=2.21, 2.83. n= 10, 11, 12). *p<0.05.

(H) Conditionally knocking out *Tph2* from DR^{Sert}→CeA neurons increases distance traveled (two-tail unpaired t-test, t=5.07, df=14. n=8, 8). ***p<0.001. Error bars, SEM. See Figures S5 and S6 for related data.

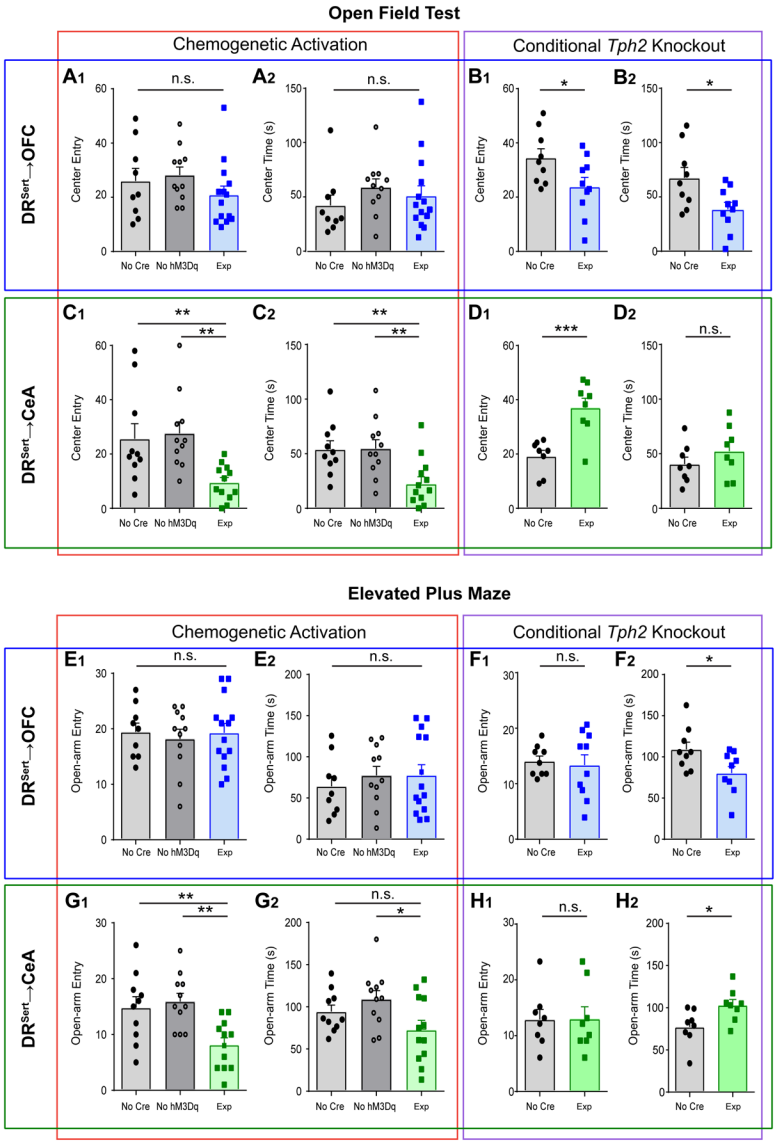

Figure 6. DR^{Sert}→CeA but Not DR^{Sert}→OFC Neurons Promote an Anxiety-like State.

(A) Chemogenetic activation of DR^{Sert}→OFC neurons does not affect the number of center entries (A_1) or time spent in the center (A_2) of the open field (one-way ANOVA, A_1, F(2, 31) = 1.23; A_2, F(2, 31) = 0.757. n= 9, 11, 14).

(B) Conditionally knocking out *Tph2* from DR^{Sert}→OFC neurons decreases the number of center entries (B_1) and the time spent in the center (B_2) (two-tail unpaired t-test; B_1, t=2.22, df=17; B_2, t=2.54, df=17. n=9, 10).

(C) Activation of DR^{Sert}→CeA neurons decreases the number of center entries (C_1) and the time spent in the center (C_2) (one-way ANOVA followed by multiple t-tests; C_1, F(2, 30) = 6.54, t=3.02, 3.17; C_2, F(2, 30) = 6.54, t=2.85, 3.30. n= 10, 11, 12).

(D) Conditionally knocking out *Tph2* from DR^{Sert}→CeA neurons increases the number of center entries (D_1), but not the time spent in the center (D_2) (two-tail unpaired t-test; D_1, t=4.31, df=14; D_2, t=1.13, df=14. n=8, 8).

(E) Activation of DR^{Sert}→OFC neurons does not affect the number of entries to the open arm (E_1) or the time spent in the open arm in the EPM (E_2) (one-way ANOVA, E_1, F(2, 31) = 0.290; E_2, F(2, 31) = 0.341; n= 9, 11, 14).
(F) Conditionally knocking out *Tph2* from DR^{Sert}→OFC neurons does not affect the number of open arm entries (F_1), but increases the time spent in the open arm (F_2) (two-tail unpaired t-test; F_1, t=0.337, df=17; F_2, t=2.45, df=17. n=9, 10).
(G) Activation of DR^{Sert}→CeA neurons decreases the number of open arm entries (G_1), and decreases the time spent in the open arm (G_2) (one-way ANOVA followed by multiple t-tests; G_1, F(2, 30) = 7.59, t=3.00, 3.60.; G_2, F(2, 30) = 3.43, t=1.51, 2.60. n= 10, 11, 12. n.s., p=0.142).
(H) Conditionally knocking out *Tph2* from DR^{Sert}→CeA neurons does not affect the number of open arm entries (H_1), but increased the time spent in the open arm (H_2) (two-tail unpaired t-test; H1, t=0.045, df=14; H2, t=2.55, df=14. n=8, 8). *p<0.05; **p<0.01; ***p<0.001. Error bars, SEM.

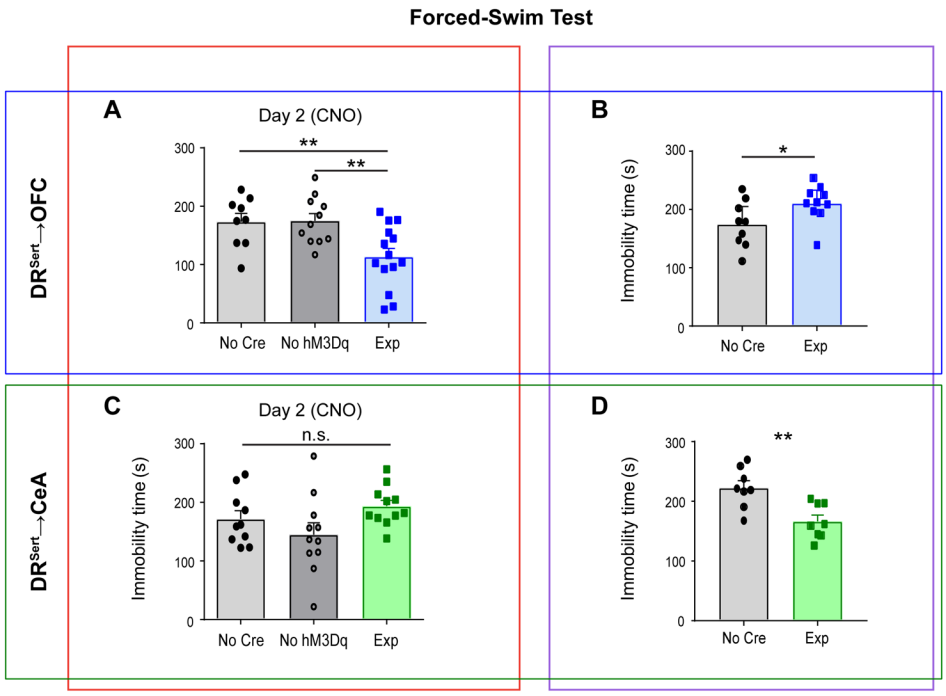

E

Behavioral Test	$DR^{Sert} \rightarrow OFC$		$DR^{Sert} \rightarrow CeA$	
	Gain-of-function	Loss-of-function	Gain-of-function	Loss-of-function
Locomotion	↓	–	↓	↑
Open Field Test (Anxiety)	–	↑	↑	↓
Elevated Plus Maze (Anxiety)	–	↑	↑	↓
Forced-Swim Test (Immobility)	↓	↑	–	↓

Figure 7. DR^{Sert}→OFC but Not DR^{Sert}→CeA Neurons Promote Escape Behavior in the Forced-Swim Test.

(A) Activation of DR^{Sert}→OFC neurons decreases the immobility time on Day 2 testing session (one-way ANOVA followed by multiple t-tests; F(2, 31) = 6.84; t=2.97, 3.24. n= 9, 11, 14). **p<0.01. See Figures S7I for related data.

(B) Conditionally knocking out *Tph2* from DR^{Sert}→OFC neurons increases the immobility time (two-tail unpaired t-test, t=2.21, df=17. n=9, 10). *p<0.05.

(C) Activation of DR^{Sert}→CeA neurons does not affect the immobility time (one-way ANOVA; F(2, 29) = 2.50. n= 10, 11, 11).

(D) Conditionally knocking out *Tph2* from DR^{Sert}→CeA neurons decreases the immobility time (two-tail unpaired t-test; t=3.58, df=14. n=8, 8). **p<0.01. Error bars, SEM.

(E) Summary of gain- and loss-of-function results.